sciendo

Contributions to Geophysics and Geodesy Vol. 48/3, 2018 (191–205)

Magnetic and Very Low Frequency Electromagnetic (VLF-EM) investigations for gold exploration around Ihale in Bunnu-Kabba Area of Kogi, north-central Nigeria

Olawale Olakunle OSINOWO*, Michael Oluseyi FALUFOSI

Department of Geology, University of Ibadan, Ibadan, Nigeria;
e-mail: wale.osinowo@ui.edu.ng, olawale.osinowo13@alumni.imperial.ac.uk;
tel.: +234 (0) 812 4109 193

Abstract: This study integrates ground magnetic and Very Low Frequency Electromagnetic (VLF-EM) methods of geophysical investigation to probe the subsurface in terms of rock magnetic susceptibility and ground conductivity for the purpose of identifying mineralized pegmatite veins that could serve as host for gold and associated metallic deposits. Twenty five (25) carefully planned ground magnetic and VLF-EM profiles, each, were occupied east and west of a reference profile which was purposively established on an identified mineralized pegmatite vein around Ihale in Bunnu-Kabba area of Kogi, north-central Nigeria. The acquired ground magnetic data were filtered and Reduced To Pole at Low Latitude (RTPLL) to remove regional field effect, cultural noise as well as focus the peaks of magnetic anomalies over corresponding sources. The measured raw real and raw imaginary components of the EM fields were subjected to Fraser and Karous Hjelt filtering to remove harmonic noise, focus and make anomaly amplitudes relate directly to the causative conductor as well as generate current density employed to characterise the subsurface. Seven (7) zones of relatively high VLF-EM derived current density with matching high residual positive magnetic anomalies present closely correlate-able signatures with subsurface response obtained around the reference profile established where local mining activities indicate evidence of gold and associated metallic mineralization of the pegmatite vein. The delineated zones constitute targets for gold and associated base metal prospects which could be further developed for economic benefit of the community.

Key words: electromagnetic survey, ground magnetic survey, gold mineralization, mineralized pegmatite veins, Ihale

*corresponding author

doi: 10.2478/congeo-2018-0008

1. Introduction

Gold is a precious and economic metal that offers rewarding financial benefit because of its precious quality and stable value. The all time high demand and the rising price of this precious metal has engendered the rush for gold in Ihale and environs in Bunnu-Kabba area of Kogi, north-central Nigeria, where low skilled local miners have built up a mining community to extract gold and other associated metals from a mineralized pegmatite vein. The success of gold extraction recorded from the various tunnels made around the vein created the interest to explore the area in order to identify other mineralized veins that could host gold and other associated metals around the study area and thus provide useful information for better organized extraction of the resource to generate tax and employment for the development of the area.

Geophysical survey is known to generate subsurface image that presents distribution of measured physical parameter(s) along the occupied profile stations and could generate 3D subsurface model where the geophysical technique sampled progressively deeper sections of the subsurface, and the data gathering done along several carefully established parallel profiles. Magnetic and Electromagnetic geophysical methods offer cheap and rapid means of gathering subsurface information about rock's magnetic susceptibility and conductivity (*Nabighian, 1991; Osinowo and Olayinka, 2013; Smith, 2014; Lymburner and Smith, 2015*). Magnetic susceptibility of rocks plays dominant influence on the intensity and inclination of the induced field generated when rocks response to the earth ambient field (*Barnett, 1976*). Variation in rock conductivity on the other hand is apt at delineating zones of preferential water saturation or occurrence of base metal deposits which often aid easy flow of current in the subsurface (*McNeill, 1990; Osinowo and Olayinka, 2012*). Careful selection of profiles that run perpendicular to the general trend of veins around the study area as well as purposive establishment of a profile as a reference profile on an established mineralized vein and the subsequent establishment of other profiles east and west of the reference profile aid identification of other pegmatite veins that could host gold and associated metallic deposits.

2. Geology of the Study Area

The study area is situated in Ihale, a settlement located few kilometres from Bunnu-Kabba area of Kogi in central Nigeria. The geology of Ihale and environs has been severally discussed to be part of the geology of south-western Nigeria which has been well described by *Oyawoye (1972), Grant (1978), Rahaman (1988)* and others. The study area consists of two main rock types which covers the area in almost equal proportions, Basement Complex rocks in the west and sedimentary rocks to the east (Fig. 1). The basement crystalline rocks include undifferentiated Basement Complex rocks which has been identified to be predominantly migmatite gneiss (comprising of augen gneiss or porphyroblastic granite and biotite gneiss) and intruded by NE–SW trending pegmatite dykes. Other common rocks include Older Granite of plutonic series of Pan African (650 Ma) tectonic events and undifferentiated meta-sediment identified as low grade schists (*Odeyemi, 1977*). The major lithology in the sedimentary terrain is sandstone, with some shale,

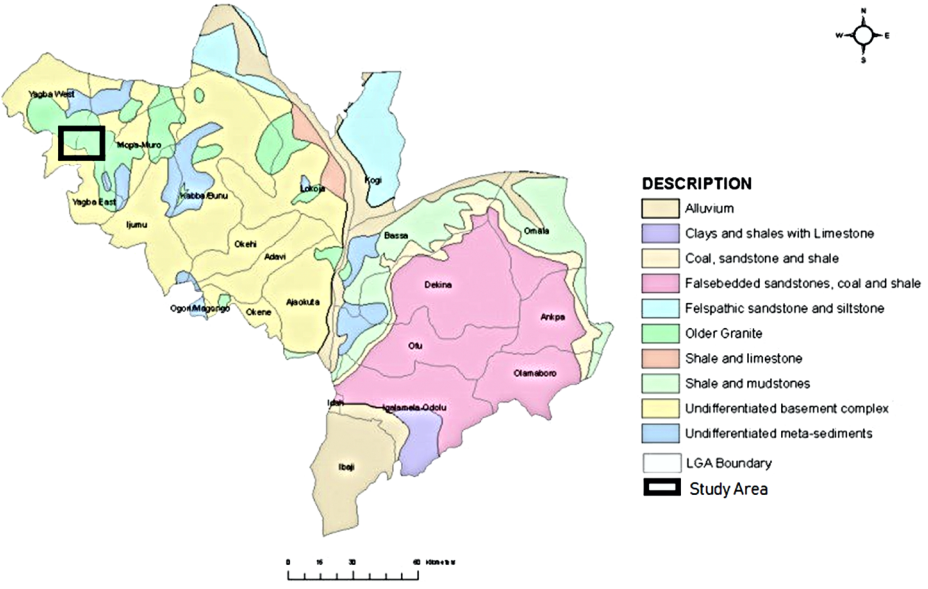

Fig. 1. Geological map of the Kogi State, North Central Nigeria; insert study area (*NGSA, 2009*).

limestone, clay and recent alluvium. The sandstones are mostly false-bedded and also contain inter-beds of coal and shale formations.

Structural imprints commonly visible on exposed rocks include foliation, namely: gneissosity, schistosity, and migmatitic banding which indicate rock strain, metamorphic differentiation and recrystallization, suggesting prolonged period of tectonic activities. Other visible structural signatures include minor faults, joints, fractures and pegmatitic intrusions emplaced within fractured zones that trend roughly NW–SE (*Ajibade, 1976*). Field evidence indicate that the pegmatites are usually granitic or granodioritic in composition with extremely coarse quartz, muscovite and feldspars grains. The pegmatite veins ranges in thickness (width) from $>$ 1 m – 10 m and sometimes measure more than 100 m in length. Pegmatites that intrude the granitic and schistose rocks around Ihale are mostly mineralized and often play host to economic minerals.

3. Materials and Methods

In this study two different geophysical investigation methods were integrated to probe the subsurface in order to delineate regions of the subsurface having mineralized veins that could serve as host for gold deposit. Two geophysical parameters were employed in this study to characterise the subsurface and they include the magnetic and the electrical properties of the earth. The magnetic method probed the subsurface in terms of magnetic elements present in metalliferous veins which based on magnetic susceptibility of different rocks delineates veins with gold mineralization. Electromagnetic method on the other hand measure ground conductivity or resistivity its inverse and due to the relative ease of electrical conduction across a mineralized vein is able to map occurrence of mineralized veins in the subsurface (*Dobrin and Savit, 1988; Eze et al., 2004; Osinowo et al., 2011*).

Ground magnetic measurements were taken using proton-precession magnetometer which consists of a simple sensor made up of a flask containing a proton-rich liquid (such as kerosene or water) unto which a magnetizing solenoid and detector coil are wound. The proton-precession magnetometer makes use of the small magnetic moment of the hydrogen nucleus (proton) to measure the precession of the proton atom to the earth magnetic field

after the current in the magnetizing solenoid coil is switched off. The measured Total Magnetic Intensity data (TMI) in nanotesla (nT) which records both the regional and the local geologic effect across the occupied profile were quality checked for spurious magnetic data such that bear no significance to the local geology. The resultant TMI data were filtered to remove out ranged, especially high frequency noise that could be attributed to cultural effects such as electric cables and surrounding metallic objects. Low pass Guassian filter was applied to remove the regional and ambient field effects. The residual magnetic data were further reduced to pole at low latitude to simplify the complex magnetic anomalies which usually characterises mid-latitude magnetic data. Here the magnetic anomalies are usually asymmetrically positioned over their causative sources due to low magnetic inclination effects at mid latitudes (*Pearson and Skinner, 1982; Keating and Zerbo, 1996; Zhang and Marangoni, 2013*). The resultant magnetic data were further filtered using Cosine roll filter to smoothen the data and remove any data processing artefact that may be introduced due to the application of other filters.

Measurement of ground conductivity to delineate mineralized veins, which often presents significantly higher conductivity value than the rocks that host them, was undertaken using ABEM WADI VLF-EM meter. The meter is apt at measuring terrain conductivity by determining the ratio of the real (Re) to the imaginary (Im) components of the propagating time varying low frequency (15–25 KHz) primary (Hp) (originating from far distant transmitting station) EM field and secondary (Hs) EM field generated when eddy current flow in subsurface conductor or conducting zone. The measured difference in field intensity and phase lag between the primary and the secondary EM field is related to the ground conductivity where a phase lag of the secondary EM field relative to the primary EM field of about half a period (180°) indicate a conducting ground, while a resistive ground (poor conductor) will cause the secondary EM field to lags the primary EM field by 90° (*Palacky, 1987; Ogilvy and Lee, 1991*).

The acquired data were quality checked (QC) to eliminate noisy data and thereafter subjected to *Fraser (1973)* filtering to generate the filtered equivalent of the raw real and the imaginary components whose anomaly peaks directly overlie the causative sources and the anomaly amplitude directly relate to the causative conductors (*McNeill and Labson, 1991*). The filters also

reduce harmonic and nonlinear noise types commonly associated with power line harmonic radiations, Global System Mobile (GSM) telecommunication transmitters and global lightening (*Park and Helliwell, 1978*). Subsequently the filtered data were subjected to *Karous and Hjelt (1983)* filtering which based on the concept that VLF-EM anomalies are caused by galvanic current response from conductive targets within the earth, transformed the measured in-phase component of the EM field into current densities at constant depths (*McNeill and Labson, 1991*). The VLFPROS MATLAB code for processing VLF-EM data developed by *Sundararajan et al. (2006)* was employed to apply *Karous and Hjelt (1983)* and thus generate 2-D pseudosection of current density (mA/cm^2) across the surveyed profiles.

Both the magnetic and electromagnetic data were collected through twenty five (25) occupied profiles which run N–S of the study area (Fig. 2). The profiles were established east and west of the reference profile at 50 m inter profile interval. The reference profile was established on a mineralized vein with evidence of gold mineralization, judging from thriving gold mining activities on the vein. Nine (9) profiles were established east (50E to 450E) of the reference profile, while fifteen (15) profiles (50W to 750W) were occupied west of the reference profile (Fig. 2). The profile range in length from 70 to 125 m and measurements were taken at 5 m station interval.

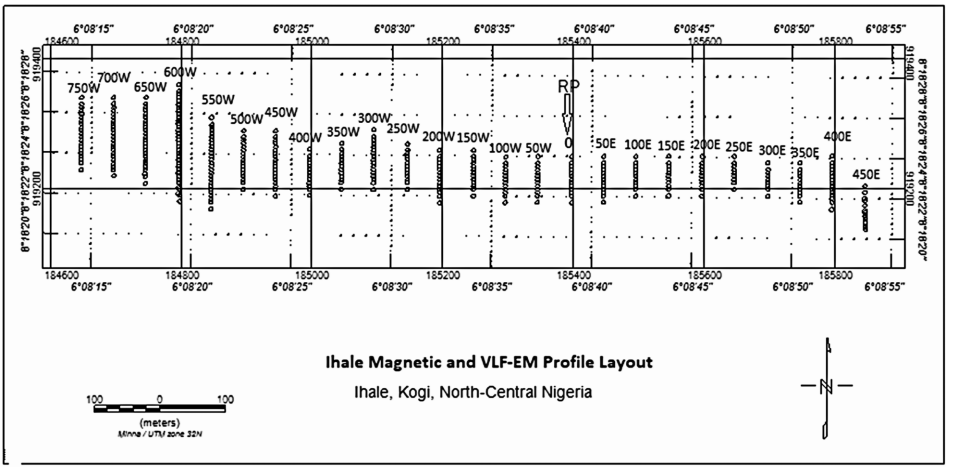

Fig. 2. Ground Magnetic and VLF-EM profile layout across the study area (RP = Reference Profile).

4. Results and Discussion

The results of the ground magnetic and VLF-EM surveys carried out for the purpose of delineating mineralized veins that could host gold deposit around Ihale in Bunnu-Kabba area of Kogi, central Nigeria are presented as 2D magnetic distribution map, 2D VLF-EM current density profile sections and 3D subsurface current density model which show the distribution of magnetic intensity and VLF-EM derived current density along the occupied profiles as well as across the study area respectively. Total magnetic intensity map of the study area is presented in the Fig. 3. The map shows the magnetic intensity due to both regional and residual magnetic fields, that is, the core or ambient field effect, as well as intensity of induced magnetic field generated by high magnetic susceptible rocks upon interacting with the earth inducing magnetic field. The residual magnetic intensity map obtained after removing regional magnetic field, filter out cultural noise, simplified and centred magnetic anomalies over causative sources is presented in Fig. 4.

The residual magnetic map indicates regions with high positive and negative amplitude anomalies as well as some medium to low positive and negative amplitude anomalies. High amplitude positive anomalies correspond to regions with relatively high magnetite rich rocks having high magnetic susceptibility (*Hunt et al., 1995*). Some of the regions that present relatively high magnetic intensity value coincide with identified mineralised pegmatite

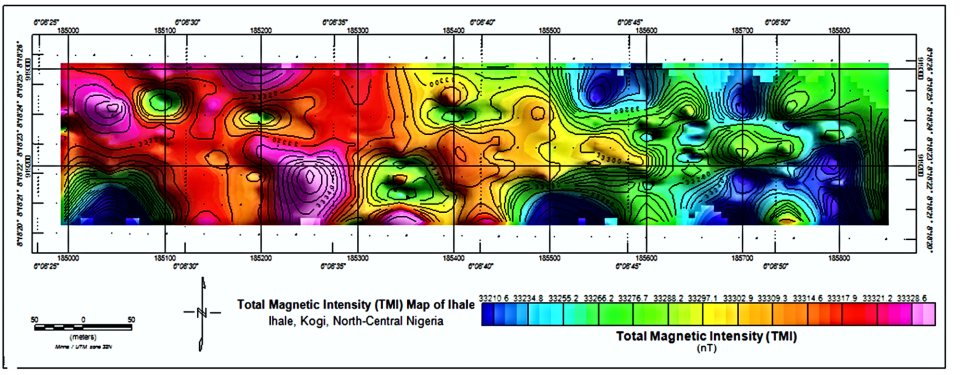

Fig. 3. Total Magnetic Intensity (TMI) Map of the study area.

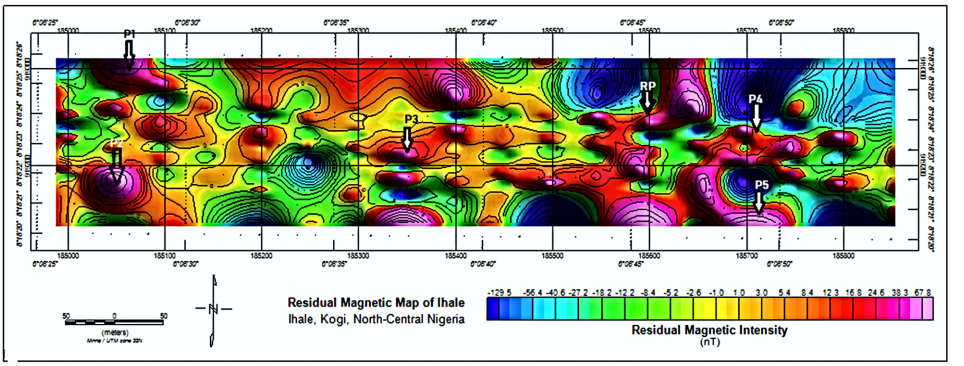

Fig. 4. Residual Magnetic map of the study area.

veins. For example, high magnetic intensity signature around the reference profile (RP arrow) coincide with pegmatite vein that triggered this survey, where local mining activities confirmed that the pegmatite vein is mineralised with base metals ores or metallic deposits of sphalerite, galena and gold.

Five (5) additional zones (P1–P5) of relatively high magnetic intensity, having magnetic signature similar to the magnetic signature of the reference vein (RP) are noticeable on the residual magnetic intensity map of Ihale. The delineated zones (P1–P5) present magnetic intensity anomaly which dominantly runs NE–SW and E–W with magnetic intensity values ranging from 45 nT to 68 nT. Three (3) of the delineated anomalous zones are situated west of the reference vein (Profile 10, Fig. 2), while the remaining two (2) occur east of the reference vein.

Two dimensional (2D) VLF-EM current density sections generated by applying *Karous and Hjelt (1983)* filter to the filtered real component of the measured VLF-EM field recorded along the occupied profiles are presented in Fig. 5(a–c). The figures show variation in current density with depth along the profile. The 2D plots imaged the subsurface in terms of current density distribution and probed up to 40 m, the depth of resolution is directly dependent on profile length. Deeper depths were resolved for long profiles while shallower depths for short length profiles. The current density has a linear relationship with ground conductivity and ranges in value from – 20 to 40 mA/cm^2 across the study area.

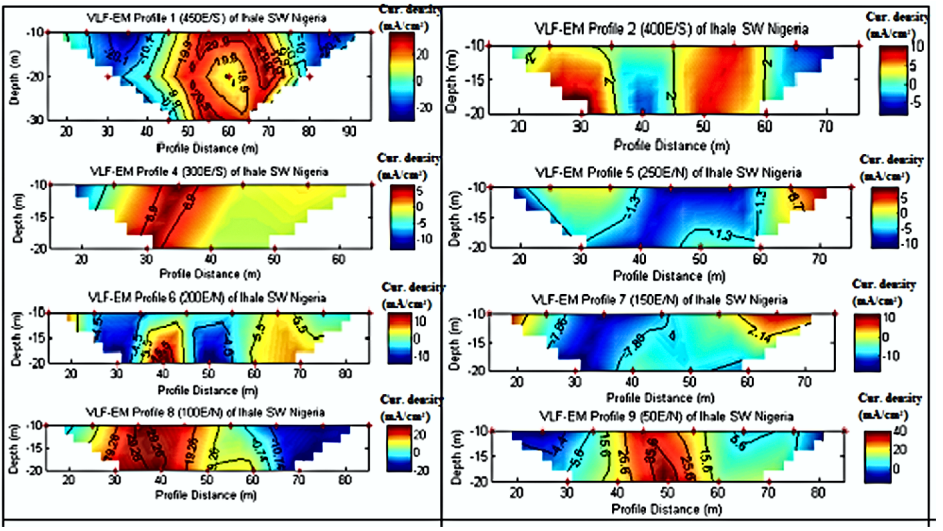

Fig. 5a. 2D VLF-EM current density sections of profile 1–9.

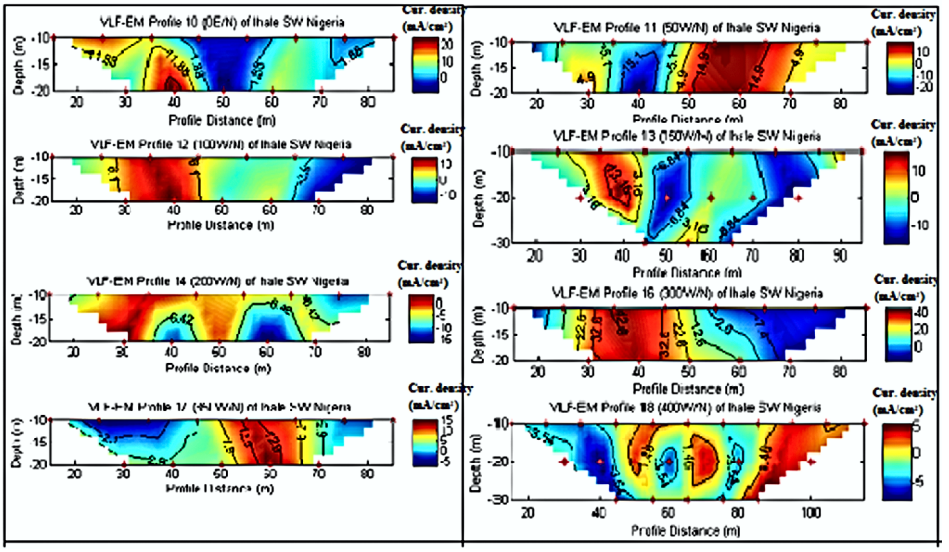

Fig. 5b. VLF-EM current density sections of profile 10–18.

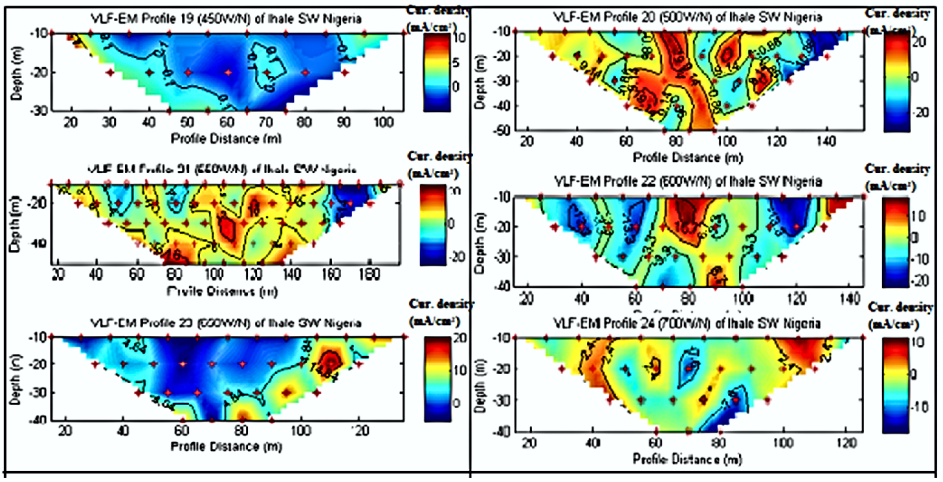

Fig. 5c. VLF-EM current density sections of profile 19–24.

Fig. 5a presents 2D current density of profiles 1 to 9 (with the exception of profile 3 which could not be resolved by the *Karous and Hjelt (1983)* filter due to very few data points) which were recorded east of the reference profile (Profile 10).

The 2D sections identified some regions of low and high current density values, with high values delineating regions of relatively high conductivity that could be attributed to occurrence of fractured zones and pegmatite veins, while region with low current density values could indicate resistive zones within the basement rocks having little or no fractures. The fractured zones and pegmatite veins are normally zones of high conductivity due to their ability to host water or metallic deposits. Fig. 5 (b & c) presents the 2D current density distribution section of the reference profile (Profile 10) as well as other profiles occupied west of the reference profile (Profiles 11–24).

The reference profile which was established on a mineralized vein shows relative high current density value (between 10 – 20 mA/cm^2) with the zone of high current density corresponding to the region of active local mining operation on the vein. Most of the delineated relatively high current density zones present a form like veins that are either inclined to the north or south of the profile which runs in north – south direction. Generally, prominent zones of relatively high current density characterise profiles close to the

reference profile while those occupied farther away present less prominent conductive zones (Fig. 5c).

Three dimensional (3D) display of VLF-EM current density obtained by combining all the VLF-EM results from all profiles across the study area is presented in Fig. 6. It presents the current density distribution along the three orthogonal (x, y, z) directions indicating the variation of the subsurface current density along N–S, E–W as well as variation with depth, up to 52.2 m. Prominent regions of high and low VLF-EM derived current density are visible on the 3D subsurface model. The 3D model indicates current density varies from – 16 to 20 mA/cm^2 across the study area with some regions of higher subsurface conductivity when compared to the background that presented resistive signatures based on the low current density values.

A section through the 3D model in the E–W direction is presented in Fig. 7 and it indicates the vertical extent of regions of high current density. The figure revealed that some of the regions of relatively high conductivity maintain their conductivity at depth which likely suggests the continuity of the pegmatite veins up to 52 m.

Zones of high current density were isolated using isosurface data clip at 18.5 current density cut-off value for the purpose of identifying zones of characteristically high conductivity that can be related to mineralized peg-

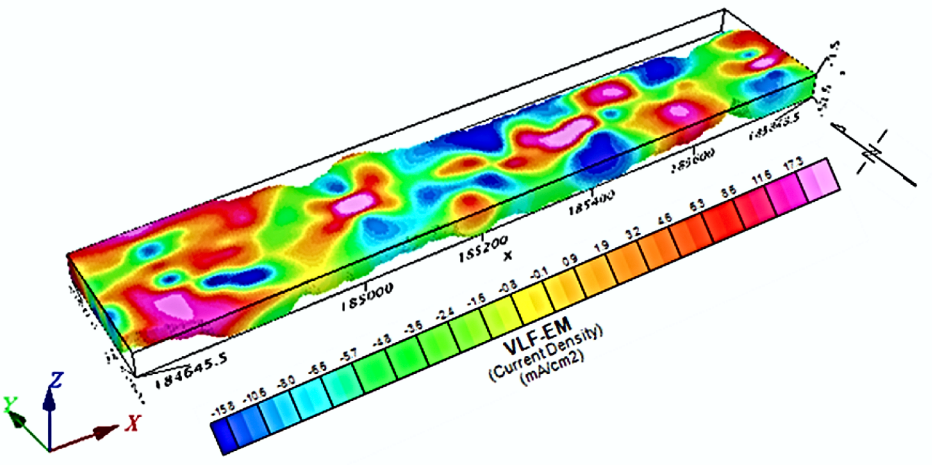

Fig. 6. 3D VLF-EM current distribution model of the surface area.

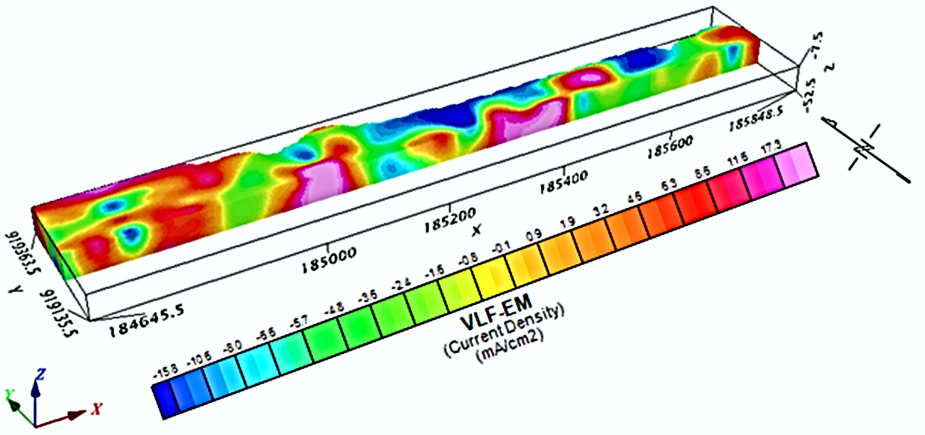

Fig. 7. E–W Section through VLF-EM 3D model of the study area.

matite veins (Fig. 8). Six (P1–P6) candidate zones of high current density ($\geq$ 18.5 mA/cm^2) were identified apart from the one that coincide with the mineralized pegmatite vein (RP) upon which the reference profile was established.

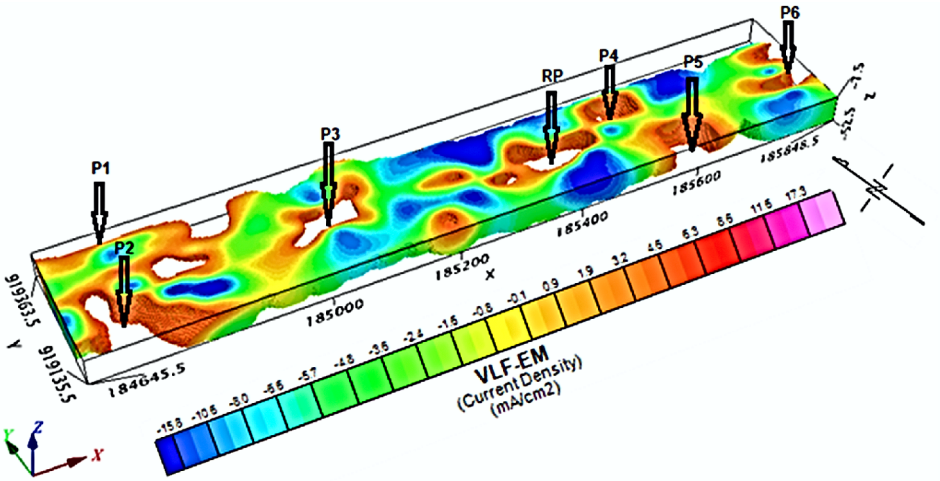

Fig. 8. Isosurface data clip at 18.5 mA/cm^2 current density cut off to delineate zones of high conductivity.

A careful examination of the generated isosurface current density data clips (Fig. 9), especially when compared with the one generated around the reference profile which was purposively established on pegmatite vein having evidence of gold mineralization in addition to other associated metallic deposits, identified six (P1–P6) other targets having similar current density signature as candidate zones for further confirmatory investigations.

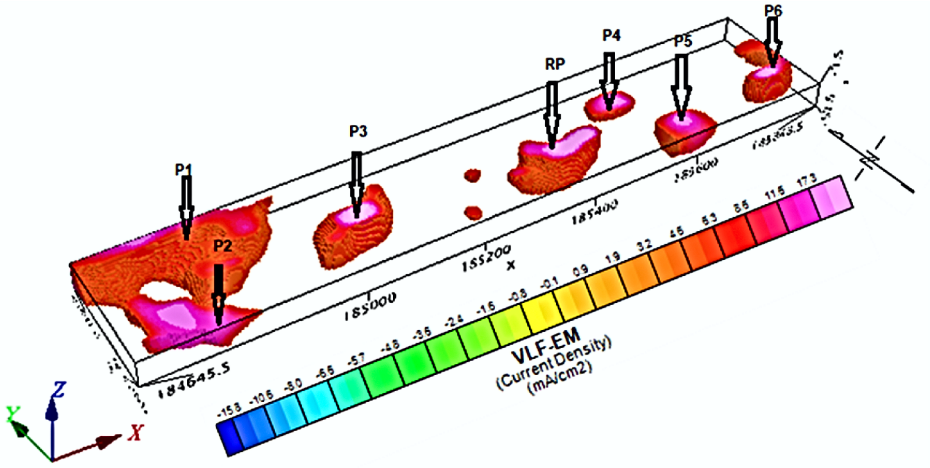

Fig. 9. Generated isosurface current density data clips (at 18.5 mA/cm^2 current density cut off).

5. Conclusion

This study highlights the importance of carefully planned ground magnetic and VLF-EM surveys for the purpose of identifying other likely mineralized pegmatite veins situated around a mineralized reference pegmatite vein upon which a measurement survey profile was purposively established. The close correlation between the magnetic and VLF-EM current density signatures between the already established mineralized pegmatite vein and other delineated zones distinguished them as targets for gold and other metallic deposits' prospect development around Ihale in Bunnu-Kabba area of Kogi, north central Nigeria.

Acknowledgements. The authors are grateful for constructive comments and suggestions of the anonymous referees, their effort helped to improve the quality of the paper.

References

Ajibade A. C., 1976: Provisional classification and correlation of the Schist belts of Northwestern Nigeria. In: Kogbe C. A. (Ed.): Geology of Nigeria. Elizabethan Pub. Co., Lagos, 85–90.

Barnett, C. T., 1976: Theoretical modeling of the magnetic and gravitational fields of an arbitrarily shaped three dimensional body. Geophysics, **41**, 1353–1364.

Dobrin M. B., Savit C. H., 1988: Introduction to Geophysical Prospecting. 4th ed., New York, McGraw-Hill, 867.

Eze C. L., Mamah L. I., Israel-Cookey C., 2004: Very low frequency electromagnetic (VLF-EM) response from a lead sulphide lode in the Abakaliki lead/zinc field, Nigeria. International Journal of Applied Earth Observation and Geoinformation, **5**, 159–163.

Fraser D. C., 1973: Magnetite ore tonnage estimates from an aerial electromagnetic survey. Geoexploration, **11**, 97–105.

Grant N. K., 1978: Structural distinction between a metasedimentary cover and an underlying basement in the 600 m.y. old Pan-African domain of north-western Nigeria. Bull. Geol. Soc. Am., **89**, 50–58.

Hunt C., Moskowitz B. M., Banerje S. K., 1995: Magnetic properties of rocks and minerals. In: Ahrens T. J. (Ed.): Rock Physics and Phase Relations. A Handbook of Physical Constraints. AGU Reference Shelf **3**, 189–204.

Karous M. R., Hjelt S. E., 1983: Determination of apparent current density from VLF measurements: Report. Department of Geophysics, University of Oulu, Finland, Contribution 89. 19 pp.

Keating P., Zerbo L., 1996: An improved technique for reduction to the pole at low latitudes. Geophysics, **61**, 131–137.

Lymburner J., Smith R. S., 2015: A procedure for collecting electromagnetic data using multiple transmitters and receivers capable of deep and focused exploration. Geophysics, **80**, 1, E1–E10, doi: 10.1190/geo2014-0251.1.

McNeill J. D., 1990: Use of electromagnetic methods for groundwater studies. In: Ward S. H. (Ed.): Geotechnical and environmental geophysics, **1**, SEG, 191–218.

McNeill J. D., Labson V., 1991: Geological mapping using VLF radio fields. In: Nabighian M. N. (Ed.): Electromagnetic Methods in Applied Geophysics, **2**, Society of Exploration Geophysicists, Tulsa, OK, 521–640.

Nabighian M. N., 1991: Electromagnetic methods in applied geophysics **2**, SEG.

NGSA, 2009: Geological Map of Nigeria. Nigerian Geological Survey Agency.

Odeyemi I. B., 1977: On the petrology of the basement rocks around Igarra, Bendel State, Nigeria. Ph. D. Thesis (unpublished), 223 p. Univ. of Ibadan, Nigeria.

Ogilvy R. D., Lee A. C., 1991: Interpretation of VLF-EM inphase data using current density pseudosections. Geophysical Prospecting, **39** 567–580.

Osinowo O. O., Akanji A. O., Akinmosin A., 2011: Integrated Geophysical and Geotechnical Investigation of the Failed Portion of a Road in Basement Complex Terrain, Southwestern Nigeria. RMZ – Materials and Geoenvironment, **58**, 2, 143–162.

Osinowo O. O., Olayinka A. I., 2012: Very Low Frequency Electromagnetic (VLF-EM) and Electrical Resistivity (ER) Investigation for Groundwater Potential Evaluation in a Complex Geologic Terrain around Ijebu-Ode Transition Zone, Southwestern Nigeria. Journal of Geophysics and Engineering, **9**, 4, 374–396.

Osinowo O. O., Olayinka A. I., 2013: Aeromagnetic Mapping of Basement Topography around the Ijebu-Ode Geological Transition Zone, Southwestern Nigeria. Acta Geodaetica et Geophysica, **48**, 3, 451–470.

Oyawoye M. O., 1972: The Basement Complex of Nigeria. In: Dessauvagie T. F. J. and Whiteman A. J. (Eds.): African Geology. Ibadan Univ. Press, Nigeria, 67–99.

Palacky G. J., 1987: Resistivity characteristics of geologic targets. In: Nabighian M. N. (Ed.): Electromagnetic Methods in Applied Geophysics – Theory, **1**, Society of Exploration Geophysicists, Tulsa, OK, 53–129.

Park C. G., Helliwell R. A., 1978: Magnetosphere effects of power line radiation. Science, **200**, 4343, 727–730, doi: 10.1126/science.200.4343.727.

Pearson W. C., Skinner C. M., 1982: Reduction-to-the-pole of low latitude magnetic anomalies, 52nd Ann. Internat. Mtg., Sot. Expl. Geophys., Expanded Abstracts, 356–358, doi: 10.1190/1.1826974.

Rahaman M. A., 1988: Recent advances in the study of the basement complex of Nigeria. In: Oluyide P. O. et al. (Eds.): Precambrian Geology of Nigeria. Geological Survey of Nigeria Publication, Kaduna, 11–43.

Smith R., 2014: Electromagnetic Induction Methods in Mining Geophysics from 2008 to 2012. Surveys in Geophysics, **35**, 1, 1230-156.

Sundararajan N., Rameshbabu V., Prasad N. S., Srinivas Y., 2006: VLFPROS—A MATLAB code for processing of VLF-EM data. Computers & Geosciences, **32**, 1806–1813, doi: 10.1016/j.cageo.2006.02.021.

Zhang H., Marangoni Y. R., 2013: A new RTP method via nonlinear thresholding at low latitudes. 13th International Congress of the Brazilian Geophysical Society & EXPOGEF, Rio de Janeiro, Brazil, 26–29 August 2013, 337–339, doi: 10.1190/sbgf2013-072.

sciendo

Contributions to Geophysics and Geodesy Vol. 48/3, 2018 (207–230)

Detection of future changes in trends and scaling exponents in extreme short-term rainfall at selected stations in Slovakia

Silvia KOHNOVÁ[1], Marianna VASILAKI[2], Martin HANEL[3], Ján SZOLGAY[1], Kamila HLAVČOVÁ[1], Athanasios LOUKAS[2], Gabriel FÖLDES[1]

[1] Slovak University of Technology in Bratislava, Faculty of Civil Engineering, Department of Land and Water Resources Management, Radlinského 11, 810 05 Bratislava, Slovakia; e-mail: silvia.kohnova@stuba.sk, jan.szolgay@stuba.sk, kamila.hlavcova@stuba.sk, gabriel.foldes@stuba.sk

[2] Laboratory of Hydrology and Aquatic Systems Analysis, Department of Civil Engineering, University of Thessally, PedionAreos, 38334 Volos, Greece

[3] Czech University of Life Sciences Prague, Faculty of Environmental Science, Kamýcká 129, 165 00 Prague 6 – Suchdol, Czech Republic

Abstract: This paper analyses projected changes in short-term rainfall events during the warm season (April – October) in an ensemble of 30 regional climate model (RCM) simulations. The analysis of trend changes and changes in scaling exponents was done for the Hurbanovo, Bratislava, Oravská Lesná, and Myjava stations in Slovakia. The characteristics of maximum rainfall events were analysed for two scenario periods, one past and one future (1960–2000 and 2070–2100) and compared to the characteristics of the actual observed events. The main findings from the analysis show that 60-min short-term events for most of the RCM simulations will either increase or remain constant. On the other hand, the depths and intensities of daily events are projected to increase significantly; in some cases they were found to be ten times larger. Trends in future events at the Hurbanovo station were found to be insignificant. In the other stations positive trends in future rainfall events prevail, except for daily rainfall at the Myjava station, which shows a negative trend. Using results from the selected simulations, the scaling exponents estimated are on average lower than the exponents of the data observed. On the other hand, due to the higher daily precipitation amounts in the future seen to all the scenarios, the downscaled values of short-term rainfall at all the stations analysed might be considerably higher in the future horizons, which could subsequently affect future design rainfall values for engineering designs.

Key words: trend analysis, scaling exponents, short-term rainfall, RCM projections

doi: 10.2478/congeo-2018-0009

1. Introduction

Changes in precipitation will be one of the most critical factors determining the overall impact of climate change. There is evidence that regions that are already wet are likely to get wetter, but details on how much wetter and what impacts there will be on a local scale are difficult to ascertain. The dry regions of the subtropics are likely to get drier and will shift towards the poles. For much of Europe, wetter winters are expected, but drier summers are anticipated over central and southern Europe. It is likely that in a warmer climate, heavy rainfall will increase and be produced by fewer but more intense events. This could lead to longer dry spells and a higher risk of floods.

The detection of trends in precipitation data is also an essential point for the assessment of changes in the water resources of a region and the impacts from climate variability. Testing the significance of the trends observed in hydrological and climatic time series has received a great deal of attention recently, especially after changes observed in the natural and human environments due to global warming. This is reflected by the huge number of studies carried out over the last three decades dealing with assessments of the significance of trends in a variety of natural time series, including temperature, evaporation, precipitation, flow, and water quality time series (*IPCC, 2007*). Several studies have analyzed extreme precipitation trends across Europe. *Madsen et al. (2014)* provided a review of the trend analysis of extreme precipitation and hydrological floods in Europe based on observations and future climate projections. They found that there is evidence of a general increase in extreme precipitation, whereas there are no clear indications of significant trends on large-scale regional or national levels of extreme streamflow. For Slovakia, *Hlavcova et al. (2015)* estimated the impact of climate change-induced extreme precipitation events on flooding. An increase in extreme 5-day precipitation totals and floods was indicated.

Another useful tool in water resources management is knowledge of the quantiles of extreme precipitation of various durations. Such information is usually expressed as the relationship between the intensity-duration-frequency (IDF) of extreme rainfall. The IDF relationship of heavy storms is one of the most important hydrological tools used by engineers for designing flood alleviation and drainage structures in urban areas. Local IDF equations

are often estimated on the basis of records of intensities abstracted from rainfall depths of different durations that have been observed at a given rainfall gauging station. In some regions, there may exist a number of rainfall gauging stations operating for a time period sufficiently long enough to yield a reliable estimation of the IDF relationships; in many other regions, especially in developing countries, these stations are either non-existent or their sample sizes are too small. Because daily precipitation data is the most accessible and abundant source of rainfall information, it seems natural, at least for regions where data at higher time resolutions are scarce, to develop and apply methods to derive the IDF characteristics of short-duration events from daily rainfall statistics.

The scaling hypothesis is a method that is able to use daily rainfall statistics in order to derive characteristics for shorter duration rainfall events, which has been the main topic of several studies during recent decades. In these studies scaling formulas were proposed to extend the IDF relationship from the usual daily time scale to shorter durations based on the scaling properties of the rainfall. *Koutsoyiannis and Foulfoula-Georgiu (1993)* used a scaling model to predict storm hyetographs. *Menabde et al. (1999)* showed that based on the empirically observed scaling properties of rainfall and some general assumptions about the cumulative distribution function for the annual maxima of mean rainfall intensity, it is possible to derive simple IDF relationships. In Slovakia the scaling properties of extreme rainfall were tested in the studies of *Bara et al. (2009)*. The authors examined the scaling properties of extreme rainfall in Slovakia in order to establish the scaling behavior of statistical moments over different durations.

The purpose of this paper is to analyze changes in extreme short-term precipitation event characteristics at four stations in Slovakia, i.e., Myjava, Bratislava, Hurbanovo and Oravská Lesná. The analysis was performed during the warm period (April–October) since the most extreme rainfall events occur in Slovakia during this period. The data used were the annual maxima rainfall values of the warm period, which were obtained by an ensemble of Regional Climate Models (RCM) within the ENSEMBLES (*van der Linden and Mitchell, 2009*) and EURO-CORDEX (*Jacob et al., 2014*) projects. The event characteristics were analyzed for two scenario periods, i.e., one past and one future (1960–2000 and 2070–2100). Historical data observed at a one-minute time step resolution were also used, so that we

could evaluate the results of the models due to future changes. Trends in the projected events were estimated and compared with the characteristics of the historical events. The scaling properties of the projected events were examined so as to estimate the scaling exponents of the future data. This paper is a follow up of a previous study, i.e., *Vasilaki et al. (2017)*, which examined changes in the seasonality of the short-term rainfall at these stations.

The paper is organized as follows: A theoretical description of the climate models used is provided in the following section. The methodology section describes the methods used to estimate the trend and scaling exponents of short-term rainfall. The study area and data sets used are described in section 3. The exposition of the results follows in the respective section. The paper is closed by a discussion and summary.

2. Methodology

2.1 Trend detection

In a number of studies parametric and non-parametric tests have been applied for trend detection. Both types of tests are commonly used; the parametric tests are more powerful, but they require data to be normally distributed and independent. On the other hand, non-parametric tests can deal with outliers within the data sets as they only require that the data be independent.

The non-parametric Mann-Kendall test (*Mann, 1945; Kendall, 1955*) is one of the most widely-used tests for detecting trends in a time series. It is based on testing the correlation of two groups of observations as proposed by *Kendall (1955)* and takes into account the correlation between the rank order of the values observed and their order over time. The null hypothesis is that the data are independent and randomly ordered, i.e., that there is no serial correlation or trend among the observations.

However, observations in time series are often autocorrelated. Simulation studies reveal that a positive autocorrelation makes it too easy to assert a significant trend, while a negative autocorrelation makes it too difficult to find a significant trend. *Cox and Stuart (1955)* stated that "positive serial correlation among the observations would increase the chance of significant

error, even in the absence of a trend". Since most series in practice exhibit a positive autocorrelation, this makes it important to check the autocorrelation in a given series and adjust the test if necessary. In this paper, the modified Mann-Kendall test proposed by *Hamed and Rao (1998)* was applied to take into account the possible presence of autocorrelation in our data.

The rank correlation test (*Kendall, 1955*) for two sets of observations $X = x_1, x_2, \ldots, x_n$ and $Y = y_1, y_2, \ldots, y_n$ is constructed as follows. The statistic S is calculated as follows:

$$S = \sum_{i<j} a_{ij} b_{ij}, \tag{1}$$

where

$$a_{ij} = \operatorname{sgn}(x_j - x_i) = \begin{cases} 1 & x_i < x_j \\ 0 & x_i = x_j \\ -1 & x_i > x_j \end{cases}, \tag{2}$$

and b_{ij} is similarly defined for the observations in Y. Under the hypothesis of independent and normally ordered data, the statistic S tends to normality for large n, with the mean and variance given by:

$$E(S) = 0\,.$$

$$\operatorname{Var}(S) = n(n-1)(2n+5)/18\,. \tag{3}$$

If the Y values are replaced by the order of the time series X, the test can be used as a trend test. In this case, the statistic becomes:

$$S = \sum_{i<j} a_{ij} = \sum_{i<j} \operatorname{sgn}(x_j - x_i)\,, \tag{4}$$

with the same mean and variance. *Kendall (1955)* gives a proof of the asymptotic normality of the statistic S. The significance of trends is tested by comparing the standardized test statistic $Z = S/[\operatorname{var}(S)]^{0.5}$ with the standard normal variate at the desired significance level.

However, when the data are autocorrelated, the variance S depends on the true autocorrelation structure, which in practice is unknown. *Hamed and Rao (1998)* propose an approximation. First, they calculate the Sen's

slope and then subtract the predicted values from the data, which is an attempt to make the series stationary. Then, the autocorrelations of the ranks of the resulting data are calculated. These are then used in calculating an approximate variance of S, which is larger if the series is positively autocorrelated. An "effective sample size", i.e., n_S^* is obtained. When the data are positively autocorrelated, n/n_S^* is greater than 1, and when the data are negatively autocorrelated, n/n_S^* is less than 1. If there is no autocorrelation, the ratio is equal to 1, and no adjustment is made. The variance of S is multiplied by the factor n/n_S^* in the test for the significance of S.

In this paper the existence and significance of trends were examined for both the past and future scenario periods and for the observed data, using the modified Mann-Kendall trend test in order to avoid delusive results due to the possible existence of autocorrelation within the data. Then comparative boxplots were constructed, in order to detect the changes in behaviour between the past and future events, as well as the differences among the stations and rainfall durations. In addition to the detection of trends during the whole time period, the moving trends and rainfall duration were also estimated for each station in order to perceive the evolution and the yearly distribution of the intense short-term rainfall and detect in trends changes points.

2.2 The simple scaling methodology

In this study, a simple scaling hypothesis was adopted in order to derive the IDF characteristics of the rainfall. The methodology applied herein follows the one used in *Menabde et al. (1999)* and *Yu et al. (2004)*. For detailed information on the theoretical background of the multifractal behavior of rainfall, the reader is referred to *Veneziano and Furcolo (2002)*, and *Lovejoy and Schertzer (1995)*, more practice-oriented results can be found, e.g., in *Gupta and Waymire (1990), Menabde et al. (1999), Yu et al. (2004)*, and *Molnar and Burlando (2008)*.

Let Id and $I\lambda d$ denote the annual maximum rainfall intensity series for the time durations d and λd, respectively. The two random variables Id and $I\lambda d$ are related through the scale factor λ (which is the ratio between the two time durations) and have the same scaling property as (*Yu et al., 2004*):

$$I_{\lambda d} \overset{dist}{=} \Lambda^{\beta} I_d \,, \tag{5}$$

where the equality is meant in the sense of the equality of the probability distributions of both variables, and β represents the scaling exponent. Such a behaviour is denoted as "simple scaling in the strict sense" (*Gupta and Waymire, 1990*).

This type of scaling implies that both variables have the same probability distribution function if the finite moments of an order q exist for both. The relationship between the q^{th} moments of rainfall intensity can be obtained after raising both sides of Eq. (1) to power q and taking the ensembles average (*Yu et al., 2004*):

$$E\left[I_{\lambda d}^{q}\right] = \lambda^{\beta q} E\left[I_d^q\right] , \tag{6}$$

where βq represents the scaling exponent of order q. The scaling exponent can be estimated from the slope of the linear regression relationships between the log-transformed values of the moments and the scale exponents for the various orders of moments. The case where the relationship between the scaling exponent and order of moment is linear is referred to as "wide sense simple scaling" (*Gupta and Waymire, 1990*).

The scaling behavior can also be found for the parameters of a fitted cumulative distribution function (CDF) if the CDF has a standardized form (*Menabde et al., 1999; Yu et al., 2004*):

$$F_d\,(i) = F\left(\frac{i-\mu_d}{\sigma_d}\right) , \tag{7}$$

where function F is independent of d. For the simple scaling process it can be shown that the statistical properties of the CDF for the two different timescales d and λd are related as follows (*Menabde et al., 1999; Yu et al., 2004*):

$$\mu_{\lambda d} = \lambda^{\beta} \mu_d \,, \tag{8}$$

and

$$\sigma_{\lambda d} = \lambda^{\beta} \sigma_d \,, \tag{9}$$

where μd (σd) is the location (scale) parameter of the annual precipitation maxima of duration d; λ denotes the scale factor; and β is the scaling

exponent. Based on these assumptions, the intensities I_d^P of events with the same annual frequency P, but a different duration d, will satisfy the scaling relation

$$I_{\lambda d}^P = \lambda^\beta I_d^P \,. \tag{10}$$

On the basis of Eq. (10), it is possible to estimate the scaling exponent even if the data record is short (*Menabde et al., 1999*).

2.3 Regional Climate Models

Regional Climate Models (RCMs) are widely used for the dynamic downscaling of Global Climate Model (GCM) simulations in order to bridge the gap between the relatively coarse resolution of GCMs (hundreds of km^2) and typical scales needed for impact studies and adequate representations of regional heterogeneity such as complex orography, land cover or land/water contrasts. RCM simulations provide high-resolution (tens of square kilometers) information that is consistent with a GCM-simulated (large-scale) climate (*Rummukainen, 2010*). Fine spatial scales provided by RCMs are especially important for precipitation, near-surface wind speeds, and key atmospheric processes, particularly those controlling the development of high-impact weather events. Information about the RCMs used in the present study is provided in the data section.

3. Study area

Slovakia is located in a mild climate zone with precipitation influenced by the Atlantic Ocean that impacts predominantly in the western part of the country; the continental influence is typical of the southeastern part. The Mediterranean climate mainly influences the southern part of central Slovakia with higher precipitation totals in the autumn.

The Sixth National Communication of the Slovak Republic on Climate Change (2013) for the period of 1880–2012 showed that a significant increase in the mean annual air temperature of 1.8 °C and an insignificant decrease in the annual areal precipitation totals by about 1.3% was recorded. The developments in temperature and precipitation were accompanied by a decrease

in relative air humidity and an increase in potential evapotranspiration by about 5% in southern Slovakia. The period of 1880–2012 was significant not only for the rapid increase in air temperature (by about 2 °C) but also for the great variability in precipitation totals (164% of the normal in 2010, 74% of the normal in 2003), which caused several episodes of serious drought on the one hand and local or regional floods on the other. The changes in the winter precipitation totals and the increase in the winter air temperature caused unstable snow conditions in Slovakia, but an increase in snow cover days and depths was recorded only in the higher mountains.

3.1 Data analysis

The measured rainfall data of the hourly time steps from the warm season (April – October) were provided by the Slovak Hydrometeorological Institute for the Myjava, Oravská Lesná, Bratislava and Hurbanovo climatological stations. The locations of the stations are presented in Fig. 1, and the basic information of the analyzed stations are presented in Table 1. The stations were selected due to the availability of the climate scenarios provided by the Czech University of Life Sciences Prague (Dr. Hanel) and also to cover the southern, northern and western parts of Slovakia, which have the longest actual observation periods of short-term rainfalls. The annual maxima rain-

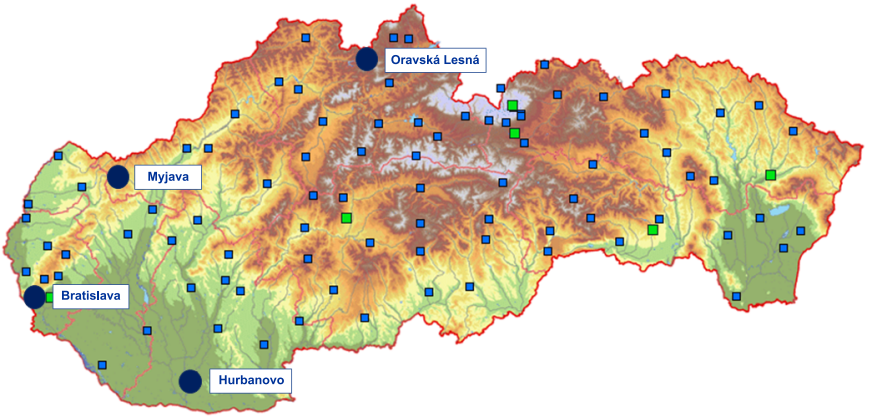

Fig. 1. The network of climatological stations in Slovakia with the locations of the analyzed stations.

fall for various durations from 60 up to 1440 min. were determined from the hourly rainfall time series measurements. For the Hurbanovo station, the observation period ranged from 1961 to 1994, while for the other stations it was from 1995 to 2009.

Table 1. Basic information about analyzed stations.

Climatological Station	Elevation [a.s.l.]	Latitude			Longitude			100-year daily precipitation [mm]
Bratislava	287	48	10	7	17	6	38	82.6
Myjava	349	48	45	14	17	33	42	72.9
Oravská Lesná	780	49	22	6	19	10	59	130.0
Hurbanovo	115	47	52	23	18	11	39	77.0

In the present study we considered an ensemble of 30 RCM simulations (see Table 2) of 3 RCMs conducted within the ENSEMBLES (*van der Linden and Mitchell, 2009*) and CORDEX (*Jacob et al., 2014*) projects in hourly

Table 2. Overview of the RCM simulations applied.

RCM	Driven by GCM	Project	Forcing	Temp Res	Spat Res
HadRM3.0 (*Collins et al., 2011*) – Met Office Hadley Centre (MOHC), UK					
HadRM3Q0_HadCM3	HadCM3Q0	ENSEMBLES	SRES A1B	1h	25 km
HadRM3Q3_HadCM3	HadCM3Q3	ENSEMBLES	SRES A1B	1h	25 km
HadRM3Q16_HadCM3	HadCM3Q16	ENSEMBLES	SRES A1B	1h	25 km
RCA4.0 (*Kupiainen et al., 2011; Samuelsson et al., 2011*) – Swedish Meteorological and Hydrological Institute (SMHI)					
RCA4_CanESM2	CCCma-CanESM2	EUR-44 CORDEX	RCP4.5, RCP8.5	20min	50 km
RCA4_CNRM-CM5	CNRM-CM5	EUR-44 CORDEX	RCP4.5, RCP8.6	20min	50 km
RCA4_EC-EARTH	ICHEC-EC-EARTH	EUR-44 CORDEX	RCP2.6, RCP4.5, RCP8.5	20min	50 km
RCA4_CM5A-MR	IPSL-CM5A-MR	EUR-44 CORDEX	RCP4.5, RCP8.5	18min	50 km
RCA4_MIROC5	MIROC5	EUR-44 CORDEX	RCP4.5, RCP8.5	20min	50 km
RCA4_HadGEM2-ES	MOHC-HadGEM2-ES	EUR-44 CORDEX	RCP4.5, RCP8.5	20min	50 km
RCA4_ESM-LR	MPI-ESM-LR	EUR-44 CORDEX	RCP4.5, RCP8.5	20min	50 km
RCA4_NorESM1-M	NCC-NorESM1-M	EUR-44 CORDEX	RCP4.5, RCP8.5	20min	50 km
RCA4_ESM2M	NOAA-GFDL-ESM2M	EUR-44 CORDEX	RCP4.5, RCP8.5	20min	50 km
RACMO2.1 (*van Meijgaard et al., 2008*) – Royal Netherlands Meteorological Institute (KNMI)					
RACMO2_ECHAM5	ECHAM5-r3	ENSEMBLES	SRES A1B	1h	25 km
RACMO2_MIROC	MIROC3.2	ENSEMBLES	SRES A1B	1h	25 km
RACMO22E (*van Meijgaard et al., 2012*) – Royal Netherlands Meteorological Institute NMI)					
RACMO22E	ICHEC-EC-EARTH	EUR-11 CORDEX	RCP4.5, RCP8.5	1h	12 km

time steps. The simulations are on a rotated longitude-latitude grid with a horizontal resolution ranging from 12×12 km (RACMO_22E simulations) to 50×50 km (RCA4 simulations). The simulations were driven by 10 GCMs under SRES A1B, RCP2.6, RCP4.5 and RCP8.5 forcing. Time series of annual maximum short-term precipitation for the past (1960–2000) and future (2070–2100) periods from grid boxes covering the climatological stations selected were considered.

To select the most appropriate scenarios for the stations selected, we contacted the climatologist prof. M. Lapin and Dr. M. Gera from the Department of Astronomy, Physics of the Earth and Meteorology, Faculty of Mathematics, Physics & Informatics, Comenius University, Bratislava, Slovakia. The final models suggested are the ones highlighted in Table 2.

First, we analyzed the values of the average intensities of the projected 60-min rainfall. The results at the Hurbanovo station are presented in Fig. 2 and compared with the average observed results, which are represented by a red line. We can see that the mean projected intensities are either almost equal to the observed values or higher, except for the projections of the RACMO2 models, which are significantly smaller. Another feature is in Fig. 3, where there is a comparison of the average daily intensities with the

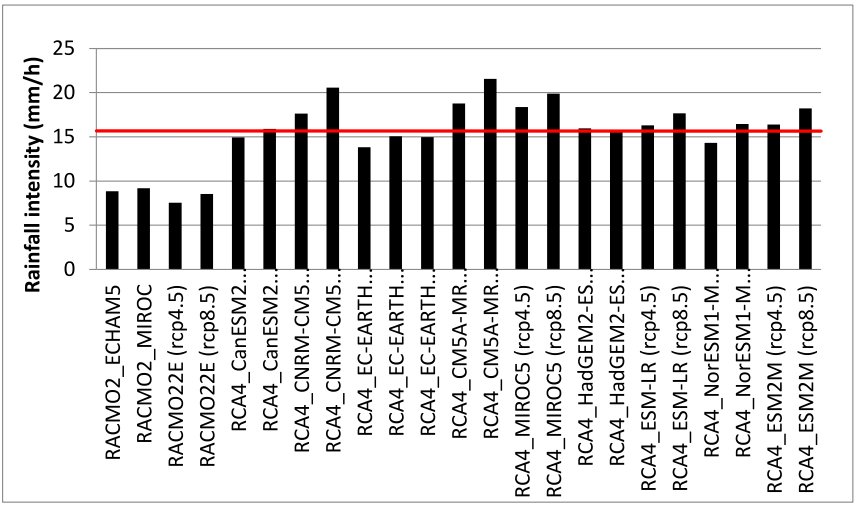

Fig. 2. Comparison of the projected 60-min rainfall intensities with the ones observed at the Hurbanovo station.

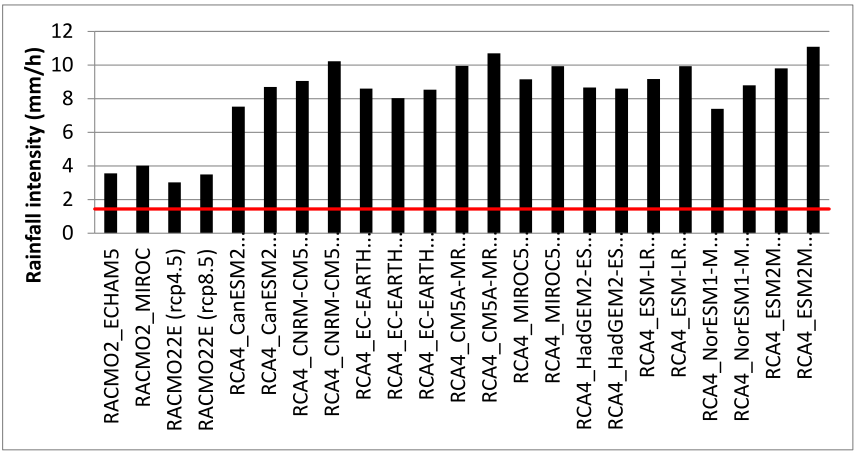

Fig. 3. Comparison of the projected daily rainfall intensities with the ones observed at the Hurbanovo station.

ones observed. All the daily rainfall projected intensities are significantly higher than the observed ones for all the stations. Similar results were also confirmed for the rest of the stations.

4. Results

As described in the methodology section, the modified Mann-Kendall trend test was applied to detect trends in the data. The significance level of the test was taken as equal to 5%. The first step was to estimate the trends using the results of all the simulations. The significant trends detected at the Myjava, Bratislava and Oravská Lesná stations are presented in the form of boxplots in Figs. 4–6, respectively. The orange box stand for the future events, while the grey one (or, in some cases, a line Fig. 6. Trends in precipitation events at the Oravská Lesná (2070–2100) with a smaller width) represents trends detected in the past events. Trends detected at the Hurbanovo station were insignificant. We can observe from the Figures that at all the stations and for all the rainfall durations, positive trends prevail, except for the daily rainfall at the Myjava station, which has a negative tendency. The range of the boxes is in some cases broader. This is due to the contradictory results of the different simulations.

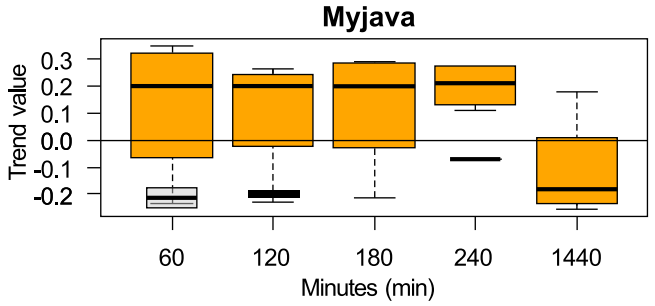

Fig. 4. Trends in precipitation events at the Myjava station (2070–2100).

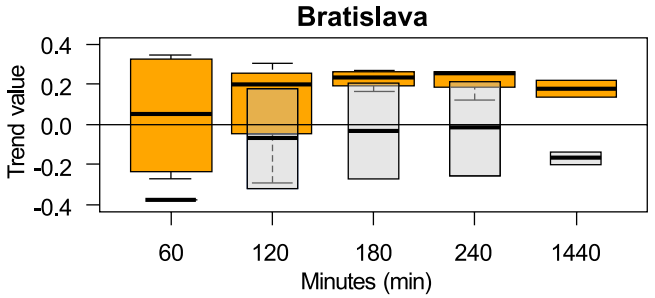

Fig. 5. Trends in precipitation events at the Bratislava station (2070–2100).

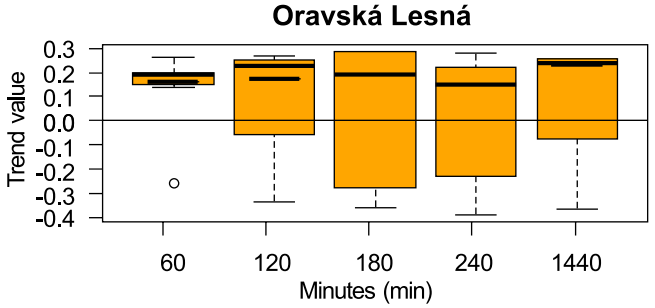

Fig. 6. Trends in precipitation events at the Oravská Lesná (2070–2100).

The next step was to examine only the behavior of the events of the selected simulations. Table 3 presents the trends estimated for all the stations. The highlighted cells represent the significant trends. Most of the long-term trends, regarding both the past and future scenarios, were found to be insignificant. The projected events of the RACMO2.1_ECHAM5 RCM ap-

Table 3. Trends in precipitation events (2070–2100, selected simulations only).

Myjava		Duration (min)				
Simulation	Scenario	60	120	180	240	1440
RCA4_ESM-LR	past	–	–	–	–	–
	rcp 45	–	–	–	–	+
	rcp 85	+	+	+	+	–
HadRM3Q0	past	NA	–	–	–	–
	fut	NA	–	–	–	–
RACMO2.1_ ECHAM5	past	–	–	–	–	–
	fut	–	–	–	–	–
RACMO22E	past	+	+	+	+	–
	rcp 45	+	–	–	–	–
	rcp 85	+	+	+	+	–
Bratislava	Scenario					
RCA4_ESM-LR	past	–	–	–	–	–
	rcp 45	+	–	+	+	+
	rcp 85	+	+	+	+	–
RACMO2.1_ ECHAM5	past	+	+	+	+	+
	fut	–	–	–	–	–
RACMO22E	past	–	–	–	–	–
	rcp 45	+	+	+	+	–
	rcp 85	+	+	+	+	+
Hurbanovo	Scenario					
RCA4_ESM-LR	past	–	–	–	–	+
	rcp 45	+	+	+	+	+
	rcp 85	+	+	+	+	+
RACMO2.1_ ECHAM5	past	+	+	+	+	+
	fut	–	–	–	–	–
RACMO22E	past	–	–	–	–	–
	rcp 45	+	+	+	+	+
	rcp 85	+	+	+	+	+
Oravská Lesná	Scenario					
RCA4_ESM-LR	past	+	+	+	+	+
	rcp 45	–	+	+	–	–
	rcp 85	+	+	+	+	–
HadRM3Q0	past	NA	+	+	+	–
	fut	NA	–	–	–	–
RACMO2.1_ ECHAM5	past	+	+	+	+	+
	fut	–	–	–	–	–
RACMO22E	past	–	+	–	–	+
	rcp 45	+	+	+	+	+
	rcp 85	+	+	+	+	+

pear to have negative trends at the Myjava, Bratislava and Oravská Lesná stations. On the other hand, future short duration events simulated by the RACMO22E RCM under the worst scenario (rcp8.5) present positive trends

at the Bratislava and Oravská Lesná stations.

To get a more thorough idea of the behaviour of the future events, we also estimated moving trends in the data. The results from each simulation present either the same or contradictory behaviour. Below we present the moving trends estimated from the projections of each RCM.

The trends estimated at the Myjava and Oravská Lesná stations using projections of RACMO2_ECHAM5 RCM were found to be insignificant for many of the cases. Projections of all the duration events of the same model for the Bratislava station show a tendency to decrease during the first 20 years (Fig. 7). For the Hurbanovo station, long-term negative trends were projected by this model for all the rainfall durations (Fig. 8).

The results of RACMO22E were almost the same for the two scenarios (rcp4.5, 8.5). At the Myjava station a large time period with significant positive trends was detected for all the rainfall durations, except for the daily one, for which the trends were not significant (Fig. 9). The behavior of the results for the Bratislava and Hurbanovo stations were similar to this in Fig. 10. Regarding the Oravská Lesná station, significant trends were only found for the daily rainfall events (Fig. 11).

The trends estimated at the Myjava station using projections from RCA4_ESM-LR for both scenarios were found to be insignificant except for those regarding the 180 and 240-min events, which appear to be negative over the long-term. The majority of trends estimated by this model at the Bratislava station were insignificant. The daily events at the Hurbanovo station projected by RCA4_ESM-LR have a positive tendency for the first 15 years of the period, while the shorter duration events have a tendency to decrease during the first 20 years of the simulation (Fig. 11). The trends found at the Oravská Lesná station were positive during the first 20 years for all the rainfall durations (Fig. 12).

4.1 Scaling

For the estimation of the scaling exponents for the future scenario period, we applied a scaling approach based on the scaling of the statistical rainfall moments. The scaling exponents were derived, including all the durations of the rainfall analyzed (60, 120, 180, 240 and 1440 min.). The property of the simple scaling of the rainfall intensities in a broad sense is demonstrated be-

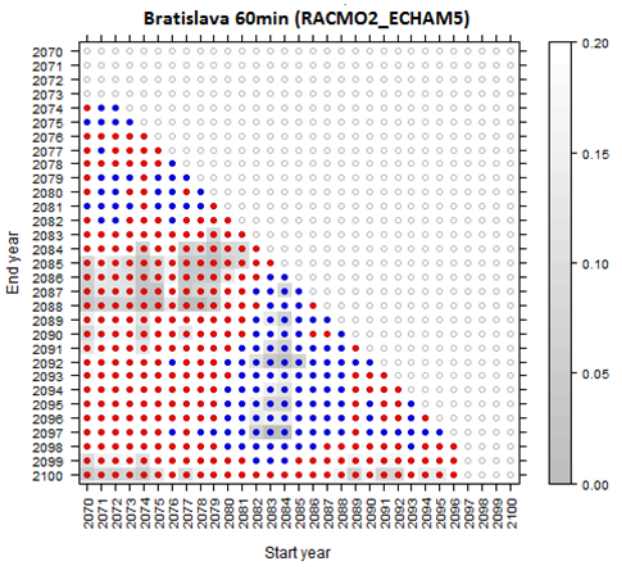

Fig. 7. Moving trends of 60-min projected rainfall at the Bratislava station (RACMO2 _ECHAM5) with significance values (grey colors).

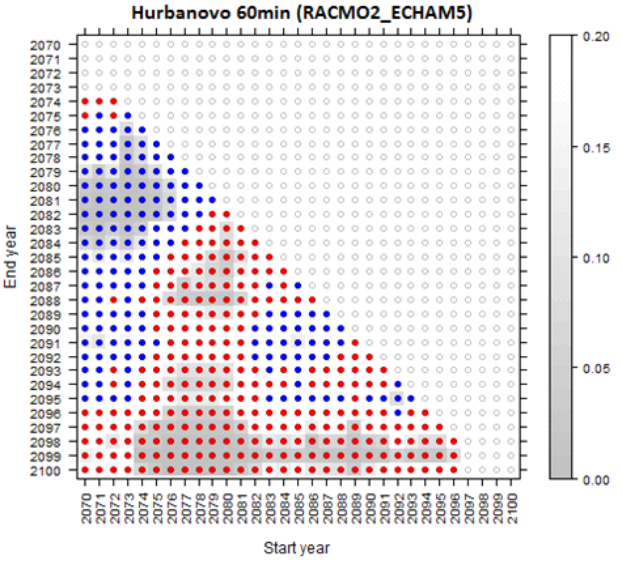

Fig. 8. Moving trends of 60-min projected rainfall at the Hurbanovo station (RACMO2 _ECHAM5) with significance values (grey colors).

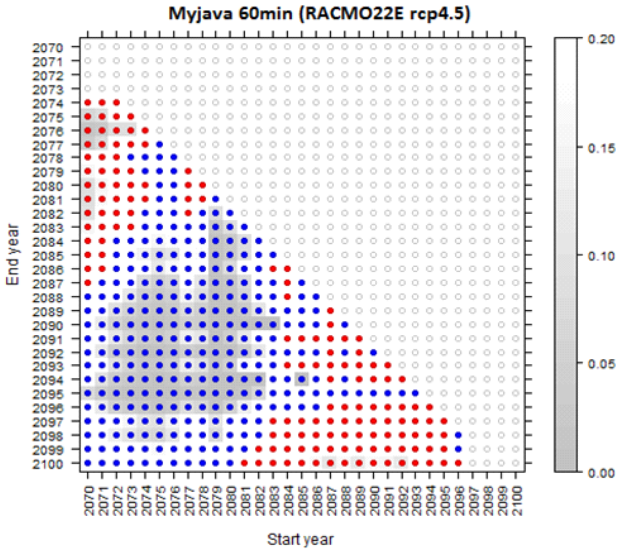

Fig. 9. Moving trends of 60-min projected rainfall at the Myjava station (RACMO22E rcp4.5) with significance values (grey colors).

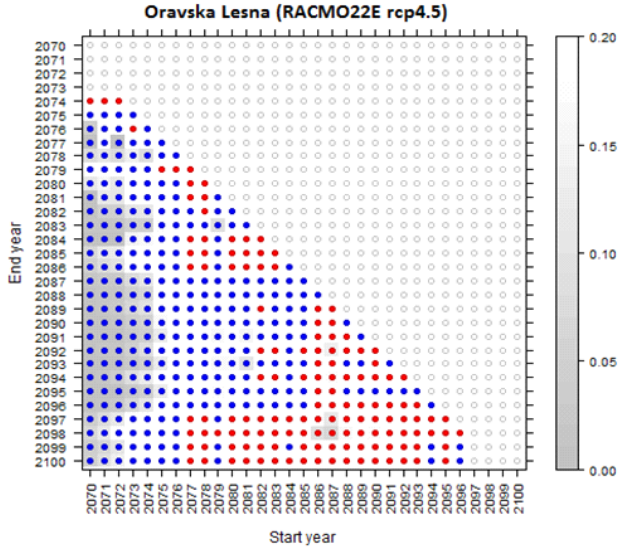

Fig. 10. Moving trends of daily projected rainfall at the Oravská Lesná station (RACMO 22E rcp4.5) with significance values (grey colors).

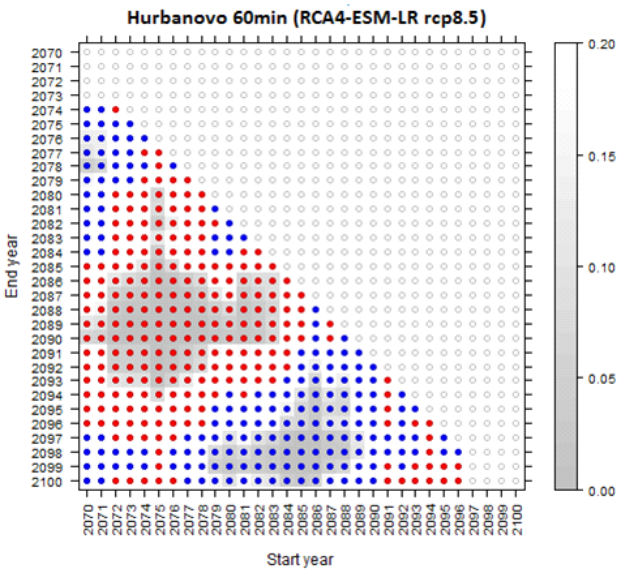

Fig. 11. Moving trends of 60-min projected rainfall at the Hurbanovo station (RCA4-ESM-LR rcp8.5) with significance values (grey colors).

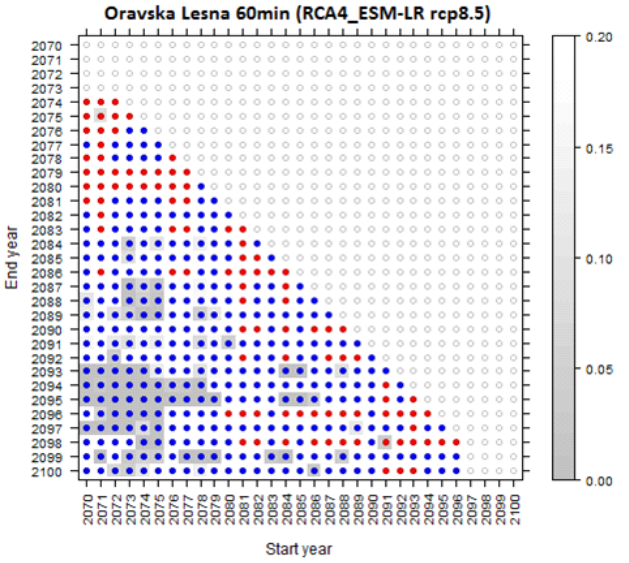

Fig. 12. Moving trends of 60-min projected rainfall at the Oravská Lesná station (RCA4-ESM-LR rcp8.5) with significance values (grey colors).

low using projections from the HadRM-3Q0 simulation. Fig. 13 displays the relationship between the log-transformed values of the moments of various orders versus various rainfall durations at the Myjava station. The scaling exponents of the moments of various orders were estimated as the slopes of the linear regression between these exponents and the rainfall durations.

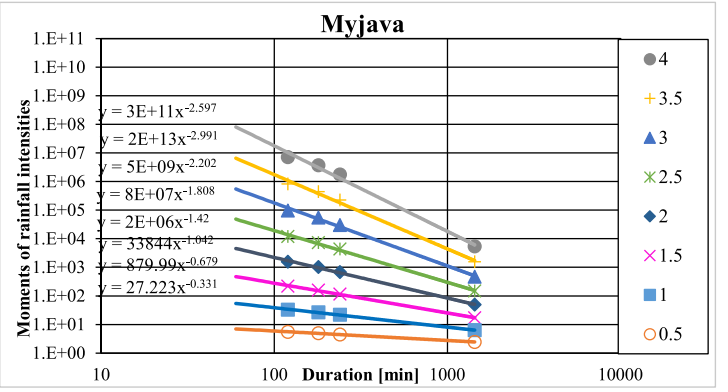

Fig. 13. Log-transformed values of moments of various orders against various rainfall durations at the Myjava station HadRM-3Q0 (SRES A1B) simulation.

Fig. 14 shows the relationship between the scaling exponents of the moments and the order of the moments. The scaling exponents decrease with the order of the moments, and a linear relationship exists between the scaling exponents and the moment orders. These two properties imply that the property of simple scaling in the broad sense exists in the stations analysed.

The same analytic procedure described above was applied to every station using the results of all the scenario simulations selected. The derived scaling exponents are presented in Table 4. The scaling exponents estimated using the results from the selected simulations prevail less than the exponents of the data observed. On the other hand, due to the higher daily precipitation amounts in the future of all the scenarios, the downscaled values of the short-term rainfall in all the stations might be considerably higher in the future horizons. This confirms the very high values of the 100-year design daily precipitation totals estimated for the future horizons using a regional approach, Table 5. For the estimation of the design precipitation values the General Extreme Value Distribution was used as the most appropriate according to the statistical tests.

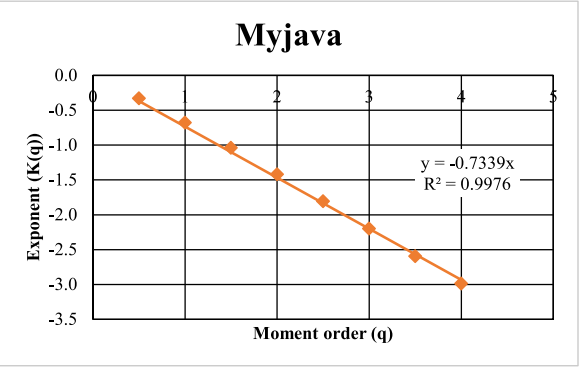

Fig. 14. Relationship between the scaling exponents of the moments and the order of the moments in the stations analysed, HadRM-3Q0 (SRES A1B) simulation at the Myjava station.

Table 4. Summary of derived scaling exponents in the stations analysed for the selected RCM scenarios.

Scenario / Clim. Station	Bratislava	Myjava	Oravská Lesná	Hurbanovo
Observed	0.7633	0.8372	0.7292	0.7713
HadRM-3Q0 (SRES A1B)	0.8176	0.7339	0.5423	–
RACMO22E-rcp4.5	0.6694	0.6880	0.6269	0.6773
RACMO22E-rcp8.5	0.6791	0.5100	0.6474	0.5490
MAX DIFF	0.0939	0.3272	0.1869	0.2223
MIN DIFF	0.0543	0.1033	0.0818	0.094

Table 5. Design 100-year daily rainfall totals for the horizon 2070–2100.

Scenario / Clim. Station	Bratislava	Myjava	Oravská Lesná	Hurbanovo
Observed	82.6	72.9	130.0	77.0
HadRM-3Q0 (SRES A1B)	123.9	160.6	190.4	–
RACMO22E-rcp4.5	150.2	181.4	155.6	167.7
RACMO22E-rcp8.5	207.5	261.5	170.8	239.3

5. Discussion

In this study we estimated the projected changes in the characteristics of the annual maxima short-term rainfall events at four stations in Slovakia:

Myjava, Bratislava, Hurbanovo and Oravská Lesná. The event characteristics were analyzed for two scenario periods, i.e., one past and one future (1960–2000 and 2070–2100), and compared to the data observed.

According to the changes in the mean characteristics of the 60-min rainfall events, we identified 3 groups of RCM simulations. The greatest part of the RCM simulations (11 out of 23) were identified as simulations with relatively unchanged rainfall intensities and depths. A considerable part of the RCM simulations (8 out of 23) show increases in 60-min event depths and intensities. Finally, the 4 RCM simulation showed decreased rainfall intensities and depths. The increases were in general more pronounced in the RCM simulations forced by RCP8.5 compared to the SRES A1B and RCP4.5 scenarios. On the other hand, all the RCM simulations project significant increases, even up to 10 times higher, in daily rainfall intensities and depths. From these results we can deduce that these RCM simulations significantly overestimate daily precipitation events. For comparison, *Jacob et al. (2014)* found statistically significant increases in total precipitation in large parts of Central Europe for the late 21st century from an ensemble of RCM simulations evaluated on a daily time scale (from the EUROCORDEX and ENSEMBLES projects). The aforementioned changes in detection were only possible for the Hurbanovo station; as for the other stations, the length of the event time-series observed was inadequate.

The uncertainties related to the RCM results are several. There are uncertainties associated with human activities, such as the emissions of greenhouse gases, and the climate system's response to increased greenhouse gas forcing, which includes climate sensitivity and feedbacks. Moreover there are uncertainties that include parameterizations and resolutions as well as initial and boundary conditions inherited from the driving global model, intermodel variability, and issues surrounding the validation or verification of the models. According to *Foley (2010)*, a simulation can never capture the complexities of an actual system. Any numerical model is limited by the knowledge the scientist has about the actual system and the computing resources available to run it. As a result, uncertainty is unavoidable in regional climate scenarios and indeed in any geographical discipline which utilizes numerical modelling.

Kendon et al. (2014) have also shown that the changes derived from models allowing for convection might be considerably different than those from

a coarser RCM resolution. Several other studies have also demonstrated the better skill of convection-permitting models in reproducing sub-daily precipitation characteristics, including the diurnal cycle and extremes (which are both closely linked to convection). Therefore, the projected changes in precipitation at short temporal scales from the current RCMs have to be interpreted with caution.

6. Conclusion

This paper provides a contribution towards the limited knowledge of possible future changes in the characteristics of sub-daily precipitation extremes that are of great importance for hydrological modelling and other applications. We analyzed future heavy rainfall event characteristics projected by an ensemble of Regional Climate Model simulations. The main findings can be summarized as follows:

- at the Hurbanovo station, for most of the RCM simulations the average 60-min event depths and intensities are projected either to increase or to remain constant. On the other hand the depths and intensities of the daily events are projected to increase significantly; in some cases they were found to be ten times larger.
- Trends in future events at the Hurbanovo station were found to be insignificant. At the other stations positive trends in future rainfall events prevailed, except for the daily rainfall at the Myjava station, which shows a negative tendency.
- The scaling exponents estimated using the results from the selected simulations were found to be lower than the exponents of the data observed on average. On the other hand, due to the higher daily precipitation amounts in the future projected by all the scenarios, the downscaled values of the short-term rainfall at all the stations analysed would be considerably higher in the future horizons.

Finally, we can conclude that these findings show a need for recalculating design short-term rainfall for the engineering practice in the future.

Acknowledgements. This study was supported by the Slovak Research and Development Agency under Contract No. 15-0497 and the Slovak Grant Agency under VEGA Project 1/0710/15.

References

Bara M., Kohnova S., Gaal L., Szolgay J., Hlavcova K., 2009: Estimation of IDF curves of extreme rainfall by simple scaling in Slovakia. Contributions to Geophysics and Geodesy, **39**, 3, 187–206.

Collins M., Booth B., Bhaskaran B., Harris G., Murphy J., Sexton D., Webb M., 2011: Climate model errors, feed-backs and forcings: a comparison of perturbed physics and multi-model ensembles. Clim. Dynam., **36**, 9–10, 1737–1766, doi: 10.1007/s00382-010-0808-0.

Cox D. R., Stuart A., 1955: Some quick sign tests for trend in location and dispersion. Biometrika, **42**, 80–95.

Foley A. M., 2010: Uncertainty in regional climate modelling: A review, Progress in Physical Geography, **34**, 5, 647–670, 24p.

Gupta V. K., Waymire E. C., 1990: Multiscaling properties of spatial and river flow distributions. Journal of Geophysical Research **95**, D3, 1999–2009.

Hamed K. H., Rao A. R., 1998: A modified Mann-Kendall trend test for autocorrelated data. Journal of Hydrology **204**, 182–196.

Hlavcova K., Lapin M., Valent P., Szolgay J., Kohnova S., Roncak P., 2015: Estimation of the impact of climate change-induced extreme precipitation events on floods. Contributions to Geophysics and Geodesy, **45**, 3, 173–192.

IPCC-TGICA, 2007: "General Guidelines on the Use of Scenario Data for Climate Impact and Adaptation Assessment. Version 2". Prepared by T. R. Carter on behalf of the Intergovernmental Panel on Climate Change, Task Group on Data and Scenario Support for Impact and Climate Assessment, http://www.ipcc-data.org/guidelines/TGICA_guidance_sdciaa_v2_final.pdf.

Jacob D., Petersen J., Eggert B., Alias A., Christensen O. B., Bouwer L. M., Braun A., Colette A., Déqué M., Georgievski G., Georgopoulou E., Gobiet A., Menut L., Nikulin G., Haensler A., Hempelmann N., Jones C., Keuler K., Kovats S., Kröner N., Kotlarski S., Kriegsmann A., Martin E., van Meijgaard E., Moseley C., Pfeifer S., Preuschmann S., Radermacher C., Radtke K., Rechid D, Rounsevell M., Samuelsson P., Somot S., Soussana J. F., Teichmann C., Valentini R., Vautard R., Weber B., Yiou P., 2014: EURO-CORDEX: New high-resolution climate change projections for European impact research. Reg. Environ. Change, **14**, 2, 563–578, doi: 10.1007/s10113-013-0499-2.

Kendall M. G., 1955: Rank Correlation Methods. Griffin, London.

Kendon E. J., Roberts N. M., Fowler H. J., Roberts M. J., Chan S. C., Senior C. A., 2014: Heavier summer downpours with climate change revealed by weather forecast resolution model. Nat. Clim. Change, **4**, 7, 570–576.

Koutsoyiannis D., Foufoula-Georgiu E., 1993: A scaling model of storm hyetograph. Water Resour. Res., **29**, 7, 2345–2361.

Kupiainen M., Jansson C., Samuelsson P., Jones C., Willén U., Hansson U., Ullerstig A., Wang S., Döscher R., 2014: Rossby Centre regional atmospheric model, RCA4, Rossby Center News Letter, Rossby Centre regional atmospheric model, RCA4.

Lovejoy S., Schertzer D., 1995: Multifractals and rain. In: Kundzewicz Z. W. (Ed.): New uncertainty concepts in hydrology and water resources. UNESCO Series in Water Sciences, Cambridge University Press, New York.

Madsen H., Lawrence D., Lang M., Kjeldsen T. R., 2014: Review of trend analysis and climate change projections of extreme precipitation and floods in Europe. Journal of Hydrology, **519**, 3634–3650.

Mann H. B., 1945: Nonparametric tests against trend. Econometrica, **13**, 245–259.

Menabde M., Seed A., Pegram G., 1999: A simple scaling model for extreme rainfall. Water Resour. Res., **35**, 1, 335–339.

Molnar P., Burlando P., 2008: Variability in the scaling properties of high-resolution precipitation data in the Alpine climate of Switzerland. Water Resources Research, **44**, W10404, doi: 10.1029/2007WR006142.

Rummukainen M., 2010: State-of-the-art with regional climate models. Wiley Interdisciplinary Reviews: Climate Change, **1**, 1, 82–96.

Samuelsson P., Jones C., Willen U., Ullerstig A., and co-authors, 2011: The Rossby Centre Regional Climate model RCAS3: model description and performance, Tellus, **63A**, 4–23.

van der Linden P., Mitchell J. F. B. (Eds.), 2009: ENSEMLES: climate change and its impacts: summary of research and results from the ENSEMBLES project. Met. Office Hadley Centre, Exeter, UK, 160 p.

van Meijgaard E., van Ulft L. H., van de Berg W. J., Bosveld F. C., van den Hurk B. J. J. M., Lenderink G., Siebesma A. P., 2008: The KNMI regional atmospheric climate model RACMO version 2.1. Koninklijk Nederlands Meteorologisch Instituut.

van Meijgaard E., van Ulft L. H., Lenderink G., de Roode S., Wipfler L., Boers R., Timmermans R. M. A., 2012: Refinement and application of a regional atmospheric model for climate scenario calculations of Western Europe. Tech. rep., KNMI, De Bilt, The Netherlands climate changes Spatial Planning publication: KvR 054/12.

Vasilaki M., Kohnová S., Hanel M., Szolgay J., Hlavčová K., Loukas A., Rončák P., 2017: Detection of future changes in seasonality in extreme short-term rainfall in selected stations of Slovakia. Contributions to Geophysics and Geodesy, **47**, 2, 133–148, ISSN 1335-2806.

Veneziano D., Furcolo P., 2002: Multifractality of rainfall and scaling of intensity-duration-frequency curves. Water Resources Research, **38**, 12, 1306, doi: 10.1029/2001WR000372.

Yu P.-S., Yang T.-C., Lin C.-S., 2004: Regional rainfall intensity formulas based on scaling property of rainfall. J. Hydrol., **295**, 1-4, 108–123.

sciendo

Contributions to Geophysics and Geodesy Vol. 48/3, 2018 (231–254)

Matlab tool REGCONT2: effective source depth estimation by means of Tikhonov's regularized downwards continuation of potential fields

Roman PAŠTEKA, David KUŠNIRÁK, Roland KARCOL

Department of Applied and Environmental Geophysics,
Faculty of Natural Sciences, Comenius University,
Mlynská dolina, Ilkovičova 6, 842 48 Bratislava, Slovak Republic;
e-mail: roman.pasteka@uniba.sk

Abstract: Transformation based on downward continuation of potential fields is an important tool in their interpretation – depths of shallowest important sources can be determined by means of stable downward continuation algorithms. We analyse here selected properties of one from these algorithms (based on Tikhonov's regularization approach) from the scope of two most important discretization parameters – dimensions of the areal coverage of the interpreted field and the sampling interval size. Estimation of the source depth is based on the analysis of computed L_P-norms for various continuation depths. A typical local minimum of these norms disappears at the source depth. We show on several synthetic bodies (sphere, horizontal cylinder, vertical rod) and also real-world data-sets (results from a magnetic survey for unexploded ordnance detection) that there is a need for relatively large surroundings around the interpreted anomalies. Beside of this also the sampling step plays its important role – grids with finer sampling steps give better interpretation results, when using this downward continuation method. From this point of view, this method is more suitable for the interpretation of objects in near surface and mining geophysics (anomalies from cavities, unexploded ordnance objects and ore bodies). Anomalies should be well developed and separable, and densely sampled. When this is not valid, several algorithms of interpolation and extrapolation (grid padding methods) can improve the interpretation properties of studied downward continuation method.

Key words: gravimetry, magnetometry, interpretation, analytical continuation

1. Introduction

Transformations of potential fields in applied geophysics (magnetic, gravity) belong among important tools in their processing and interpretation.

doi: 10.2478/congeo-2018-0010

These transformations, in general, do not directly determine field sources, but they can often provide insights that help to understand the natures of sources (*Blakely, 1995, p. 311*). Analytical continuation in source free area is one of the most important procedures among them. In general, we usually speak about upward continuation (UC, in direction away from the sources) and downward continuation (DC, in the direction closer to the sources). Downward continuation is an important procedure in potential fields interpretation – it can be utilized for two main purposes (*Mudretsova and Veselov, 1990a, p. 328*) approximation of the interpreted field on: a) depth level, which is closer to the sources and b) estimation of the sources positions/depths. On the other hand, it is an instable operation (amplifying noise and errors in data) and it must be treated in a special way.

This contribution is focused on the DC transformation as a tool for sources depths estimation in applied geophysics. It tries to present some of important properties of DC method from the aspect of its practical application. From the theoretical point of view, potential fields described by continuous functions and defined on domains with infinity dimensions, can be continued in the source free area down to the upper boundary of the shallowest source (*Baranov 1975, p. 32–33*). But in the real world these two important conditions are not valid: our data are not continuous (we work with discrete digital datasets) and they are not defined on areas with infinite dimensions (our exploration areas are always limited). Accepting this, we should analyse the properties of stable DC algorithms from the scope of two most important discretization parameters – dimensions of the areal coverage of the interpreted field and the sampling interval size. This is valid for profile data and also areal data-sets (grids). We show the important role of these two parameters on the results of used DC algorithm (focused on source depth estimation), presented on several synthetic model studies and real-world datasets interpretation (magnetic survey for UneXploded Ordnance detection). Together with our analysis we present here a software solution of all the discussed aspects – a Matlab script REGCONT2, which is an upgrade of our previously published program REGCONT (*Pašteka et al., 2012*). It can be used for an effective determination of sources depths in applied gravimetry and magnetometry (Matlab script is free for academic and scientific use).

2. Tikhonov's regularization approach in stable downward continuation

Downward continuation of potential fields is an instable operation due to its inherent properties as a high-pass filter (in Fourier domain the spectral characteristic of this operation is an exponential function of the wave-number). From practical point of view it means that any error and/or noise (in the original data) will be strongly boosted during this transformation. This is valid also for the edge effect (Gibb's phenomenon), which then often flows into strong artificial oscillations in the DC data-sets (see e.g. the Fig. 1 in *Pašteka et al., 2012*). These disturbances (oscillations) can even mask the field anomalies itself. There have been published several interesting methods for finding a stable solution of this problem (e.g. *Fedi and Florio, 2002; Trompat et al., 2003; Cooper, 2004*) and during the last years there can be followed something like a "boom" in this scientific area (e.g. *Ma et al., 2013; Zeng et al., 2013; Zhang H. et al., 2013; Abedi et al., 2014; Zeng et al., 2014; Zeng et al., 2015; Zhang Y. et al., 2016, Zhou et al., 2018; Florio and Fedi, 2018; Zhang et al., 2018*).

In our contribution we work with the classical approach from *Tikhonov et al. (1968)*, using the regularization approach in Fourier wavenumber domain (exact derivation of the spectral characteristics of the regularized downward continuation is given in the Appendix). Some authors use for this approach the abbreviation TRDC method (Tikhonov Regularized Downward Continuation; *Zhang H. et al. 2013*) or simply TR method (Tikhonov Regularization; *Zhang Y. et al., 2016*). Main idea of this approach is to use a special filter form (Eq. A.6) in the wavenumber domain, which combines the classical downward continuation spectral characteristics (exponential function) multiplied with a low-pass filter. Properties of this low-pass filter are controlled by the value of regularization parameter α, where the lower values mean lower role of regularization, higher values cause intensive damping of the high spectral content of the downward continued data. The classical challenge (as in other regularization methods) is to find an optimum value of the regularization parameter α, for which some kind of equilibrium between the original nature of the transformation (DC) and the smoothing effect of the low-pass filter occurs. In the traditional Tikhonov's method, C-norms of the solutions for different values of regularization parameter α have been constructed and interpreted (*Tikhonov et al., 1968; Glasko et al., 1970*).

From functional analysis we know that the C-norm is equal to L_∞-norm. These norms compare two adjacent solutions (obtained for two adjacent values of regularization parameter) and plot their distance (C-norm) as a function of the regularization parameter α. This is plotted as a log-log graph with the regularization parameter α on the horizontal axis and the C-norm value on the vertical axis. These norms have always been constructed for a large interval of regularization parameter α. In most of the cases are the values of α ranging from 10^{-20} to 10^{+20} m^{-1}, in a geometrical sequence with usual factor of 1.1. Their typical shape is convex and positive with the existence of a local minimum in the vicinity of their global maximum. This local minimum reports on the occurrence of the mentioned equilibrium and the optimum regularization parameter value is bound to this local minimum. This idea is very close to the concept of L-curve (*Lawson and Hanson, 1974; Hansen, 2007*), which is used in many regularization methods in mathematical physics. Appearance and disappearance of the local minimum can be used for the source depth estimation in the TRDC method – vanishing of this local minimum during downward continuation to larger depth levels points to the depth of the source (e.g. *Tikhonov et al., 1968; Glasko et al., 1970; Pašteka et al., 2011, 2012*). We can say in other words: when we enter with the continuation depth into a non-harmonic space (into the sources), method cannot find a correct solution (local minimum vanishes). Of course that the source depth depends in this method on the source shape – for vertically elongated bodies it is the top, for isometric bodies it is the centre. Our small contribution to the classical TRDC method was the way that we construct beside the classical C-norm also other L_P-norms (*Pašteka et al., 2012*). We usually calculate L_2-norms, L_1-norms and $L_{0.5}$-norms and then we select that type of norm, where the local minima are well developed (with sharper side parts of curves). It is interesting that in some situations give these other L_P-norms better results than the classical C-norms. At the moment, we are not able to scientifically explain the reason, why some kinds of norms work better in some situations – we simply try all of them and then we select the best one.

In Fig. 1 we have displayed results for the depth estimation of two simple synthetic models – a 2D horizontal cylinder with circular cross-section (depth of the cylinder centre is 1000 m) and a sphere (depth of the sphere centre is 5 m). The step in DC was for the case with horizontal cylinder

200 m and in the case with sphere 1 m. In the graphs of displayed C-norms (Fig. 1b and 1e), a nicely developed local minima are visible (with sharp side parts of curves) and detected local minimum disappear exactly at corresponding DC depths, where the most important source points of both bodies are positioned (centres of them). In Fig. 1c and f it is shown (with a detailed step in DC) that the disappearance occurs on depths, which are very close to the source position – method can focus on these details in a very detailed way – any reasonable small step of the depth change can be selected. But to speak here about some kind of the depth resolution is not appropriate, because the precision of the method depends on discretization parameters of the interpreted field (as it will be given later). This example belongs to the so-called "text-book" cases – everything works perfectly here. Why? Because the interpreted synthetic fields were evaluated

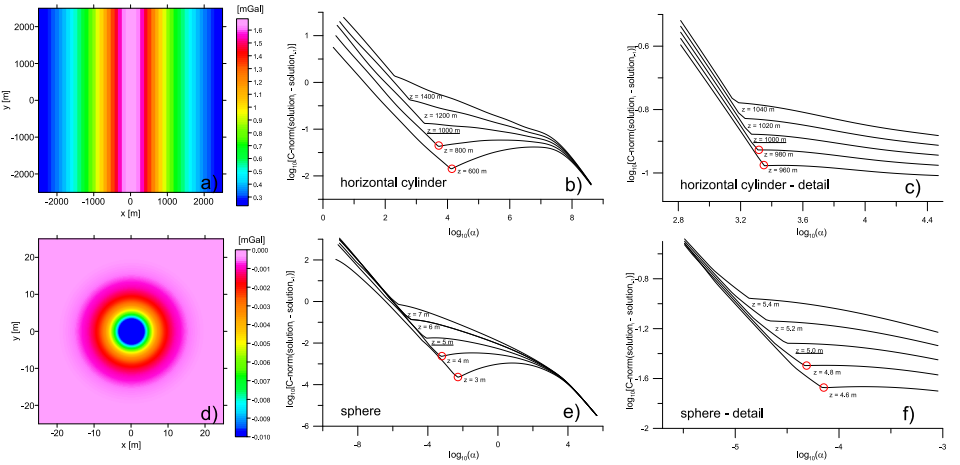

Fig. 1. Results of depth estimation for 2D horizontal cylinder and sphere. a) Synthetic vertical component of gravitational acceleration field (V_z) for the horizontal cylinder in the depth of 1000 m, b) C-norms obtained from the depth estimation of horizontal cylinder depth (depths from 600 to 1400 m, step = 200 m), c) C-norms for depths close to the source position (depths from 960 to 1040 m, step = 20 m), d) synthetic vert. component of gravitational acceleration field (V_z) for the sphere in the depth of 5 m, e) C-norms obtained from the depth estimation of sphere depth (depths from 3 to 7 m, step = 1 m), f) C-norms for depths close to the source position (depths from 4.6 to 5.4 m, step = 0.2 m). Sampling steps of the input grids are in the case of the cylinder: $\Delta x = \Delta y = 100$ m, in the case of the sphere: $\Delta x = \Delta y = 0.5$ m. Density of the 2D cylinder: $+1000\ \mathrm{kg\,m^{-3}}$, density of the sphere: $-1000\ \mathrm{kg\,m^{-3}}$.

on an area with satisfactory large dimensions (its length in both directions is 5 times the source depth) and the anomalous field is properly sampled (anomaly half-width is given by tens of grid points). But what will happen, when these two important aspects (anomalous field areal dimensions and sampling step) will not have such "ideal" values? We can see a representative example in Fig. 2 (slightly inclined sub-vertical rod with the top in 10 m depth): in the case of under-sampled data with small areal dimensions (Fig. 2c and 2d) the estimated source depth is incorrect – it is too shallow

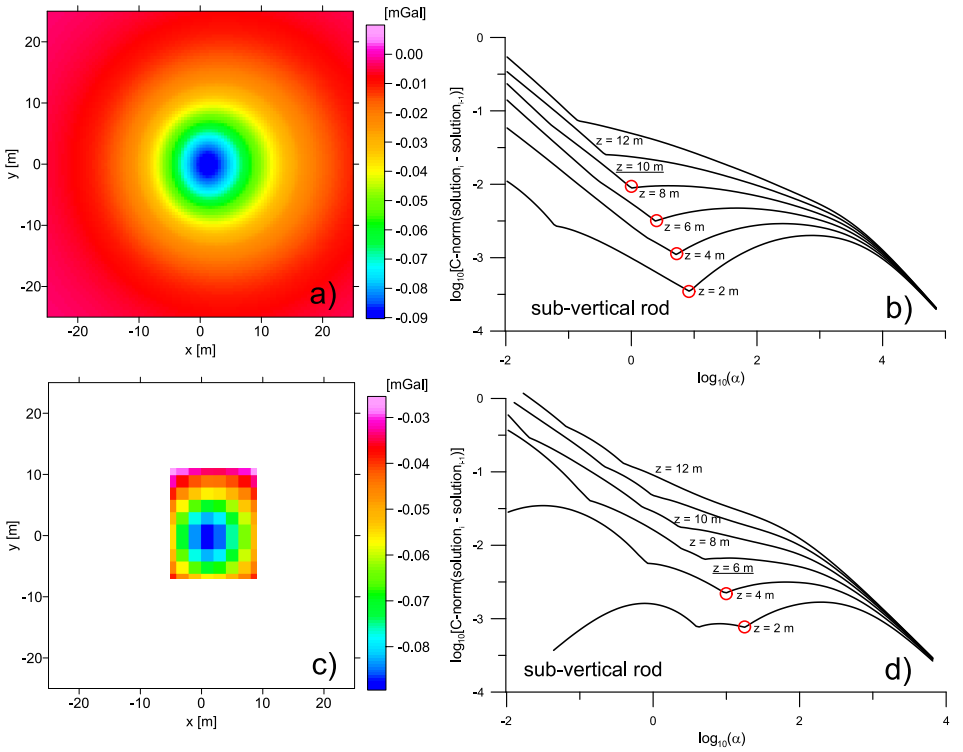

Fig. 2. Results of depth estimation for an inclined sub-vertical rod with the top in the depth of 10 m – a "good and bad" example: a) Synthetic vertical component of gravitational acceleration field (V_z), calculated on larger area (50×50 m size) with small sampling step: $\Delta x = \Delta y = 0.5$ m, b) corresponding C-norms obtained from the depth estimation, c) synthetic vert. component of gravitational acceleration field (V_z), calculated on small area (10×10 m size) with large sampling step: $\Delta x = \Delta y = 2$ m, b) corresponding C-norms obtained from the depth estimation. Density of the inclined sub-vertical rod: $-2000\ \mathrm{kg\,m^{-3}}$.

(6 m instead of correct 10 m). Shapes of the C-norms in Fig. 2d are not well developed and these graphs do not possess the necessary sharp minima in their shapes. For a comparison we give also a result for well sampled field with large dimensions (Fig. 2a and 2b) – here the corresponding C-norms are well developed and the source depth (10 m) is correctly estimated.

We had experienced not well developed C-norms and other L_P-norms in various situations and were wondering what could be the reason of that. Therefore, we started a set of experiments with these two important parameters – dimensions of the field area and its sampling steps. Results of these experiments will be shown later in this paper.

3. Software realization of TRDC method for source depths estimation – Matlab script REGCONT2

For the practical use of the proposed TRDC algorithm we have developed a Matlab script REGCONT, which was published together with our paper *Pašteka et al. (2012)*. This script is suitable for UC and DC transformation of profile and grid potential data, but it is quite cumbersome for source depth estimation – user had to evaluate the corresponding L_P-norms for each depth of continuation and then plot all these output norms separately in some another software (or in Matlab) with the aim to detect the continuation depth, where the local minimum in analysed L_P-norms disappears. From this reason, we have decided to develop a new feature called "Source Depth Estimation" tool (SDE), which became part of the new version REGCONT2. Beside this, we have updated the main computational core of the script into a vector form, which significantly speed up the script. User can choose within the SDE tool the type of used L_P-norm (C-norm, L_2-norm, L_1-norm or $L_{0.5}$-norm) and parameters of the downward continuation process: minimal depth, maximal depth and the step of depth change (see Fig. 3). After the realization of all calculations, selected norms are plotted for all continuation depth levels and in the norm graphs local minima are automatically detected and marked by a red circle. Position of the local minimum is determined by means of a simple 3-point operator, which starts on each plotted norm from the left-hand edge of the graph. Proposed Matlab script REGCONT2 is free for academic and scientific use and it can be downloaded together with supporting files and a user manual from the server:

http://www.kaeg.sk/vyskum/projekt-vega-2014/project-vega-1-0462-16/.

In the next part of our paper we analyse on a simple synthetic model (a sphere) discussed important numerical aspects of interpreted fields (anomalous field areal dimensions and sampling step size) and give also suggestions, how to solve problems in cases, when these parameters are not sufficient. Further we present few experiences with real world data-sets (magnetic surveys for UneXploded Ordnance detection).

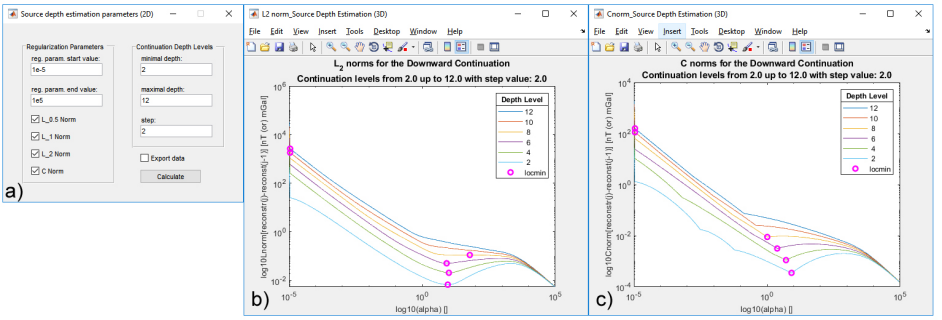

Fig. 3. Working environment of the "Source depth estimation" tool application in the frame of REGCON2 Matlab script. a) Selection of L_P-norms and continuation depths, b) displayed L_2-norms, c) displayed C-norms. Small circles in graphs of displayed norms represent automatically detected local minima in their shapes.

4. Synthetic model – sphere in gravimetry

We demonstrate the discussed properties of the classical Tikhonov's regularized downward continuation (TRDC) algorithm on the anomalous gravitational field of a sphere (depth of its centre = 1000 m, radius = 200 m, density contrast = 1000 kg m^{-3}) for various dimensions and sampling intervals of the downward continued fields. Our first trials were focused on the influence of the sampling size of the grid element (this is valid also for profile step). In general, it is valid that interpreted anomalies have to be well sampled – at least with 10 (and more) points within the half-width of the anomaly. We can see in Fig. 4a and 4b that for small sampling steps ($\Delta x = \Delta y = 100$ m, $\Delta x = \Delta y = 200$ m), displayed C-norms have very well developed sharp local minima, which disappear at the correct depth = 1000 m. This is not the

case for larger sampling steps ($\Delta x = \Delta y = 250$ m, $\Delta x = \Delta y = 500$ m) in Fig. 4c and 4d – local minima are not well developed and cannot be therefore used for depth estimation. Such a behaviour was realized also in the case of other simple geometrical shapes, as horizontal cylinder and vertical rod (not shown in this paper). It seems that this could be "a deep hit" to the TRDC method, but there exist a relatively easy solution (numerical) for this problem – interpolation. With relatively simple interpolation methods, offered in used commercial software (e.g. Golden Software Surfer, Matlab) we can re-grid the original dataset to a more dense grid and try to apply the TRDC method anew (with displaying several types of L_P-norms). From our experiences, the well-known Kriging (*Cressie, 1991*) and Minimum Curvature methods (*Smith and Wessel, 1990*) give the best results. In Fig. 5 we can see results from an experiment, where we took the grid from Fig. 4d (with parameters $\Delta x = \Delta y = 500$ m) and have re-gridded it to new grids

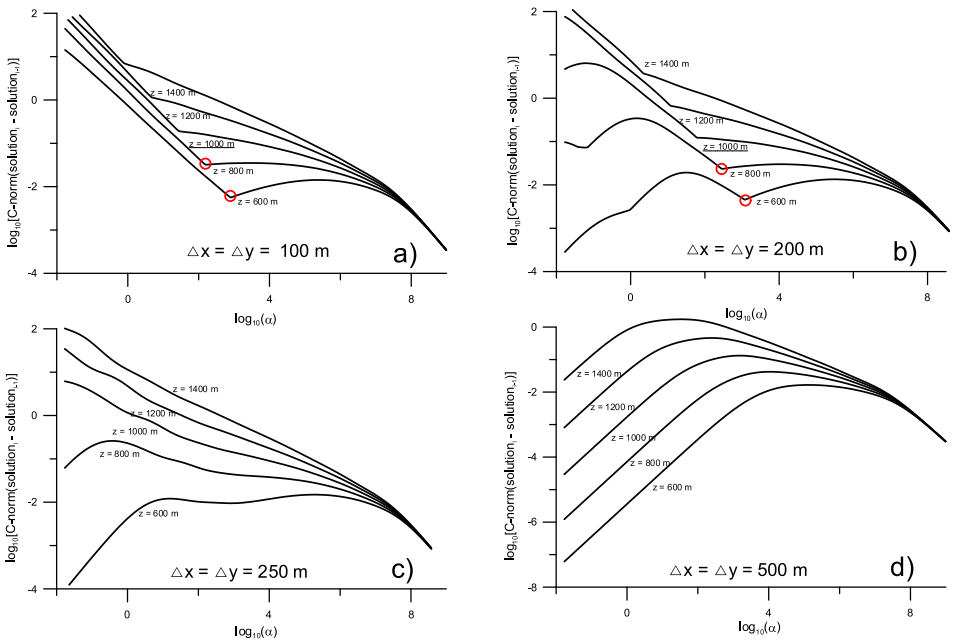

Fig. 4. Graphs of evaluated C-norms for the sphere model (grid dimensions for all cases: 5×5 km) calculated for different sampling steps: a) $\Delta x = \Delta y = 100$ m, b) $\Delta x = \Delta y = 200$ m, c) $\Delta x = \Delta y = 250$ m, d) $\Delta x = \Delta y = 500$ m. Density of the sphere model: $+1000\ \mathrm{kg\,m^{-3}}$.

with parameters $\Delta x = \Delta y = 200$m and $\Delta x = \Delta y = 100$m, using two typical interpolation methods: Kriging and Minimum Curvature. We can see that results for the Kriging method give results with quite well developed local minima in L_1-norms (Fig. 5a and 5c), which can be used for source depth estimation (local minima are not so sharp as in Fig. 4a and 4b, but can be detected by the simple automatic 3-point operator). Second interpolation method (Minimum Curvature) did not work so well in this case (Fig. 5b and 5d).

Next trials work with the areal dimensions of interpreted grids (this is valid also for profile lengths). In general, it is valid (e.g. from the total normalized gradient method, *Elysseiva and Pašteka, 2009*) that in DC methods the dimension of the grid should be 5 to 10 times larger than the expected

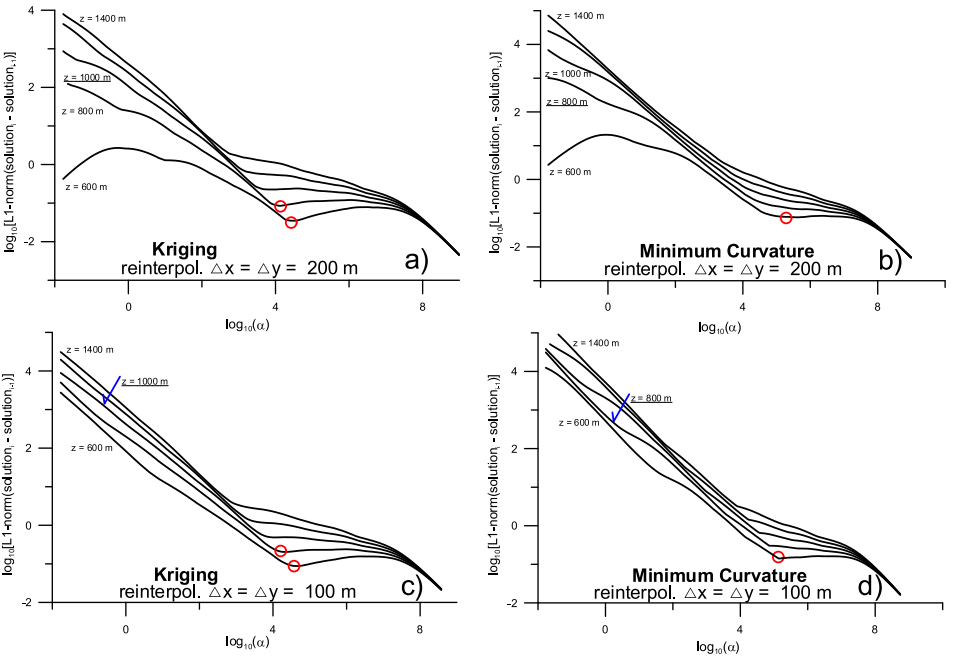

Fig. 5. Graphs of evaluated L_1-norms for the sphere model (grid dimensions for all cases: 5×5 km) calculated for different sampling steps and different interpolation methods, used for re-gridding the original data: a) $\Delta x = \Delta y = 200$ m (Kriging method), b) $\Delta x = \Delta y = 200$ m (Minimum Curvature method), c) $\Delta x = \Delta y = 100$ m (Kriging method), d) $\Delta x = \Delta y = 100$ m (Minimum Curvature method). Density of the sphere model: $+1000\,\mathrm{kg\,m^{-3}}$.

source depth. This is a quite large size and we cannot usually separate isolated anomalies with such a large (anomaly free) surroundings. But also here, there exist a solution, which helps sometimes. But let us start with our experiment results. In Fig. 6 we can see results for grids with 3 different areal dimensions: 2×2 km, 3×3 km and 4×4 km (sampling step is quite detailed and identical for all of them: $\Delta x = \Delta y = 100$ m). For smaller grid dimensions, the TRDC method works not well (Fig. 6b and 6d), local minima can be found almost on each depth level and the interpreted depth is over-estimated. For larger dimension, the method gives correct result (Fig. 6f) (here we can see that it was enough, when the grid size was 4 times larger than the source depth). Situation with small grid sizes can be quite hard for an unexperienced user, but the best way is to try several grid sizes and compare the results. Enlargement (expansion) of the grid can be realized by means of various extrapolation (padding) methods. We have tested few methods for the extrapolation of smaller grids to larger dimensions. We have realized that traditional interpolation methods (Kriging, Minimum Curvature, Radial Basis Functions, Inverse Distance method) are not suitable for larger expansions of grids (Fig. 7c and 7d), because there occurs always some kind of data deformation in the expanded grid. Also the well-known and used extrapolation approach – the cosine-taper padding method do not work properly for such large extrapolation of data (Fig. 7e). We have found a very interesting approach introducing 5 different numerical methods, coming from sparse linear algebra, which is used for interpolation and extrapolation of 2D digital data-sets (*D'Errico, 2012;* also published on Mathworks File Exchange). This approach can use various methods of approximation yielding a system of linear equations, solved then by means of sparse linear algebra methods (*D'Errico, 2018,* personal communication). User has to try several methods and then visually check, which is giving the best results. During performing experiments with data sets in the frame of this paper, we had best experiences with method nr. 3, which is based on partial differential equation approximation, using finite difference approximation. As we can see, extrapolated grid in Fig. 7f is in a very good agreement with the synthetic data, evaluated for the same area (Fig. 7b) – here we have also used the mentioned third method. In Fig. 8 we can see two examples with expanded grids TRDC interpretation, when using again the third method (extrapolation to dimensions 3×3km and 4×4km). Obtained

results are very similar to that from synthetic data experiments (Fig. 6d and 6f). We can see that also here an acceptable result was obtained for the grid with larger dimensions (4×4 km) – displayed C-norms show vanishing of the local minimum for the correct depth = 1000 m (Fig. 8d).

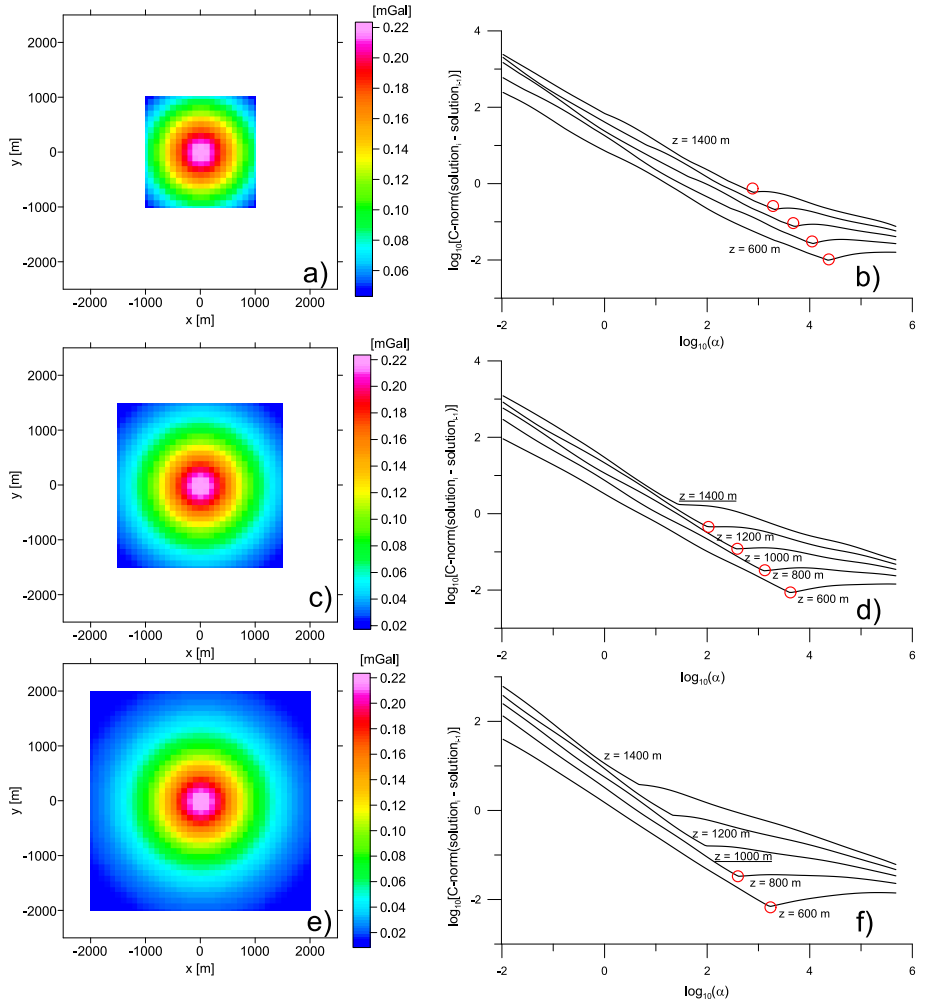

Fig. 6. Grids and graphs of evaluated C-norms for the sphere model (sampling steps for all cases: $\Delta x = \Delta y = 100$ m) calculated for different dimensions of interpreted grids: a) 2×2 km, b) corresponding C-norms, c) 3×3 km, d) corresponding C-norms, e) 4×4 km, f) corresponding C-norms. Density of the sphere model: $+1000\ \mathrm{kg\,m^{-3}}$.

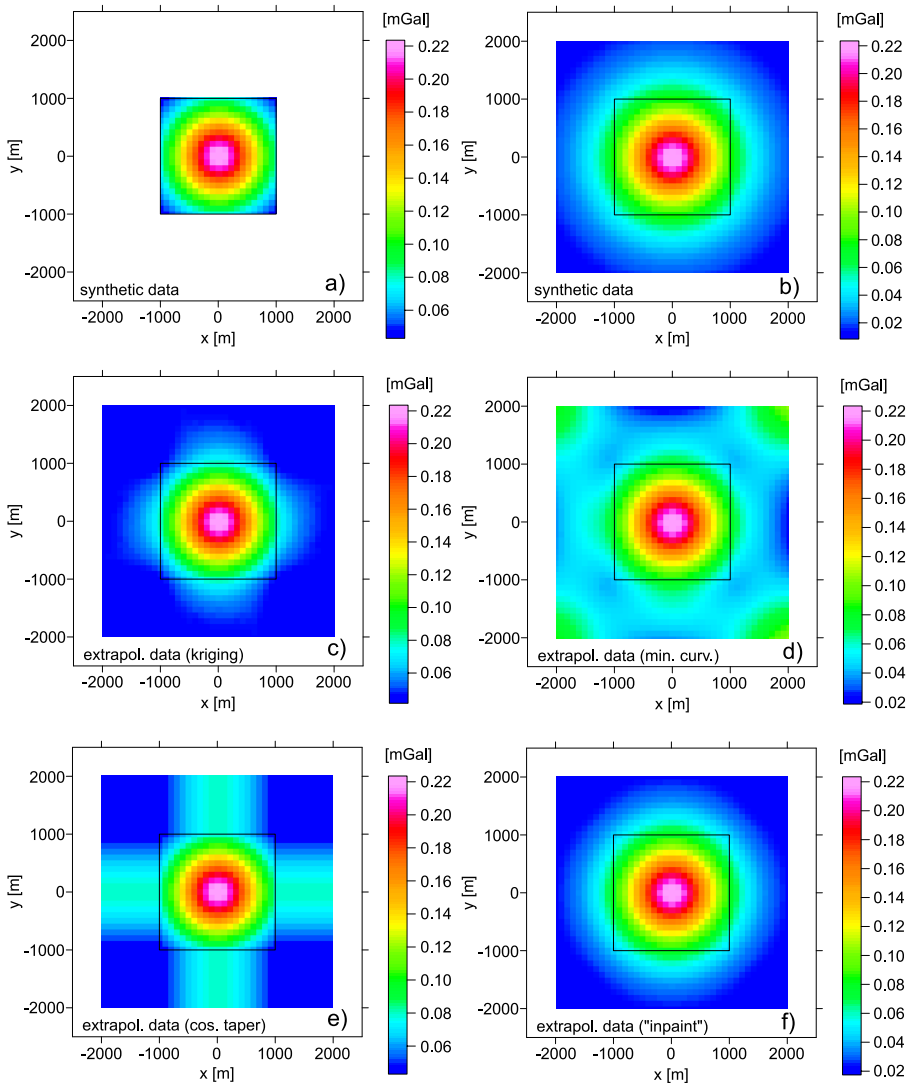

Fig. 7. Examples of expanded grids, using various extrapolation and padding methods, vertical component of gravitational acceleration field for a sphere: a) original synthetic data, grid with 2×2 km dimension (used for extrapolation), b) synthetic data, larger grid with 4×4 km dimensions, c) extrapolated grid to 4×4 km (Kriging method), d) extrapolated grid to 4×4 km (Minimum Curvature method), e) extrapolated grid to 4×4 km (Cosine-taper method), f) extrapolated grid to 4×4 km (partial differential equations approximation). Density of the sphere model: $+1000\,\mathrm{kg\,m^{-3}}$.

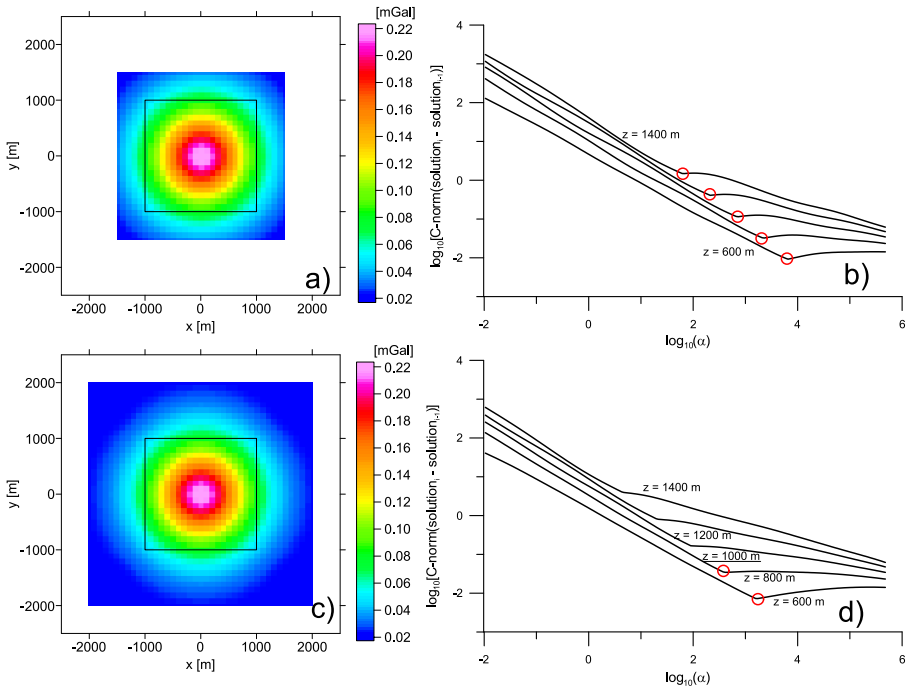

Fig. 8. Two examples of expanded grids (partial differential equations approximation) together with their corresponding C-norms: a) extrapolated to 3×3 km, b) corresponding C-norms, c) extrapolated to 4×4 km, d) corresponding C-norms. Sampling steps for all cases: $\Delta x = \Delta y = 100$ m.

5. Real world data interpretation – high definition UXO detection study

As we have shown in our synthetic examples and as it follows from our experience with real data-sets interpretation, TRDC method is suitable for the interpretation of well developed and separable anomalies from isolated and compact source bodies. In near surface geophysical applications, the search for UneXploded Ordnance (UXO) object by means of high-definition magnetic survey produces often such kind of anomalies (interesting study of regularized DC algorithm application for UXO magnetic data interpretation is given by *Li et al., 2013*). Here we bring two examples from such a type of survey. In the first example the depth of the ordnance object was

known and test measurements have been realized over it (ordnance was positioned at the earth surface). In the second example, we have selected one real anomaly from a performed UXO survey in SW Slovakia (site Rohožník-Studienka), where the detected objects have been excavated by professional pyrotechnicians. In both examples, the amplitude of the total magnetic induction field (T) was acquired by means of a Cs-vapour magnetometer with a sampling step along measured lines equal to 0.1 m. Anomalous field ΔT was obtained by means of median filter application along measured lines. In the first example, the distance between the measured lines was 0.5 m, in the second one it was 1.0 m. In both examples the ordnance was a 100 mm diameter tank projectile.

In Fig. 9 we can see results from the first experiment. When a larger

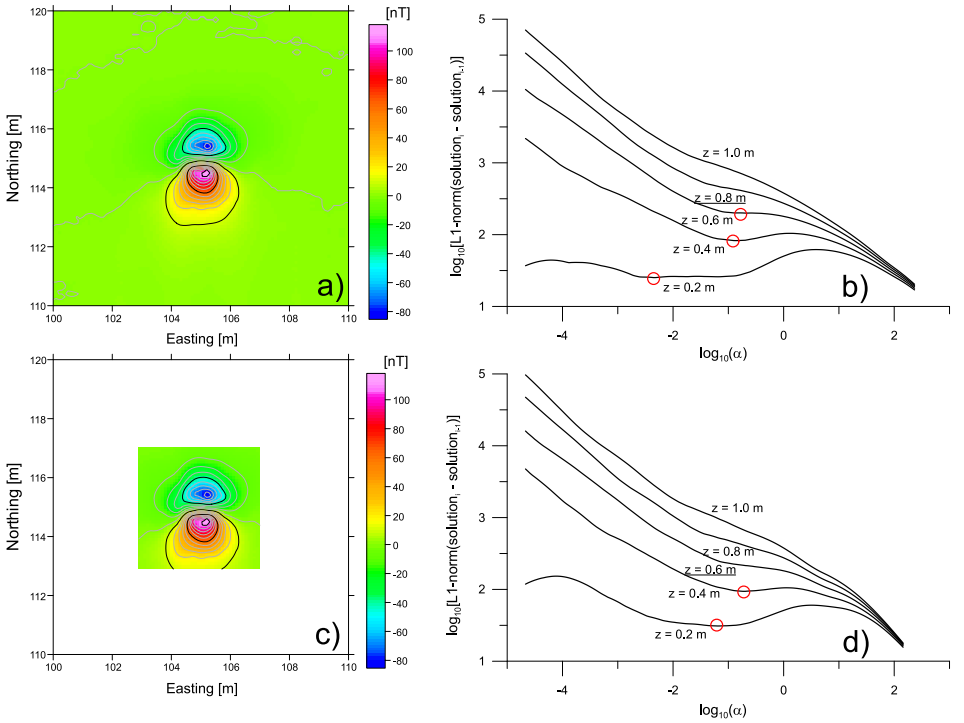

Fig. 9. Real world magnetic data-set, anomalous ΔT field over a 100 mm tank projectile, in the depth 1.0 m below the sensor: a) measured data on 10×10 m area, b) corresponding L_1-norms, c) extracted data on 3×3 m area over the projectile, d) corresponding L_1-norms. Sampling steps for all cases: $\Delta x = \Delta y = 0.1$ m.

surrounding of the anomaly has been selected (10 × 10 m area, Fig. 9a), then a larger depth of the estimated source was obtained (0.8 m) (Fig. 9b). When compared with the real depth (1.0 m), there is an error of 20%, which is acceptable in this kind of depth-estimations. In the case of an extracted (smaller) grid – (3 × 3 m area, Fig. 9c), the estimated depth is shallower (0.6 m) (Fig. 9d). For the interpretation L_1-norms have been selected, although shapes of their local minima do not have the perfect "sharp" shape (as we have seen in the case of synthetic data-sets interpretation). This is often the case, when we work with the real-world data-sets.

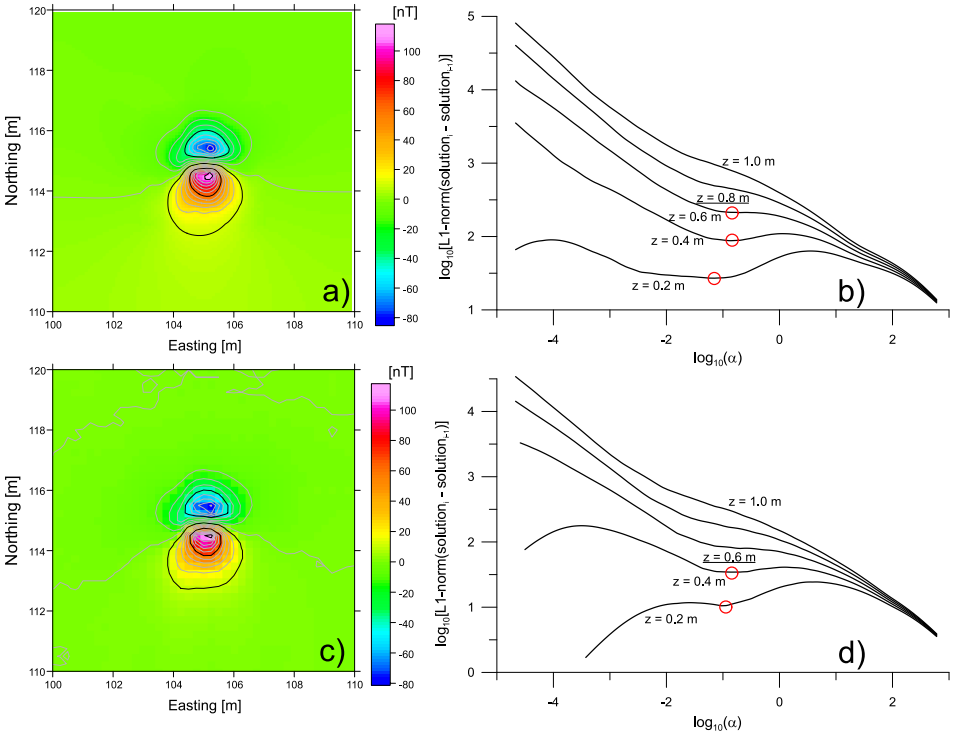

Fig. 10. Real world magnetic data-set, anomalous ΔT field over a 100 mm tank projectile, in the depth 1.0 m below the sensor: a) extrapolated data on 10 × 10 m area (from 3 × 3 m area in Fig. 9c by means of partial differential equations approximation), b) corresponding L_1-norms, c) re-interpolated measured data on the original 10 × 10 m area, d) corresponding L_1-norms. Sampling steps: for case a): $\Delta x = \Delta y = 0.1$ m and for case c): $\Delta x = \Delta y = 0.25$ m.

In Fig. 10a we can see an extrapolated grid (with the same sampling step $\Delta x = \Delta y = 0.1$ m), which was extrapolated from 3×3 m area (Fig. 9c) to 10×10 m area by means of the mentioned partial differential equations together with sparse linear algebra approach (*D'Errico, 2012*), using the method nr. 3. It can be easily seen that the L1-norms interpretation in the case of this extrapolated grid brought very similar results (Fig. 10b) like it was in the case of original data in Fig. (9b) – it resulted again to the depth of 0.8 m. In Fig. 10c we show as an addition the effect of a coarse sampling step – the original data on the area of 10×10 m have been re-grided with a sampling step $\Delta x = \Delta y = 0.25$ m, which resulted again to a shallow depth of 0.6 m (Fig. 10d).

Final example comes from real UXO survey in an area close to an ac-

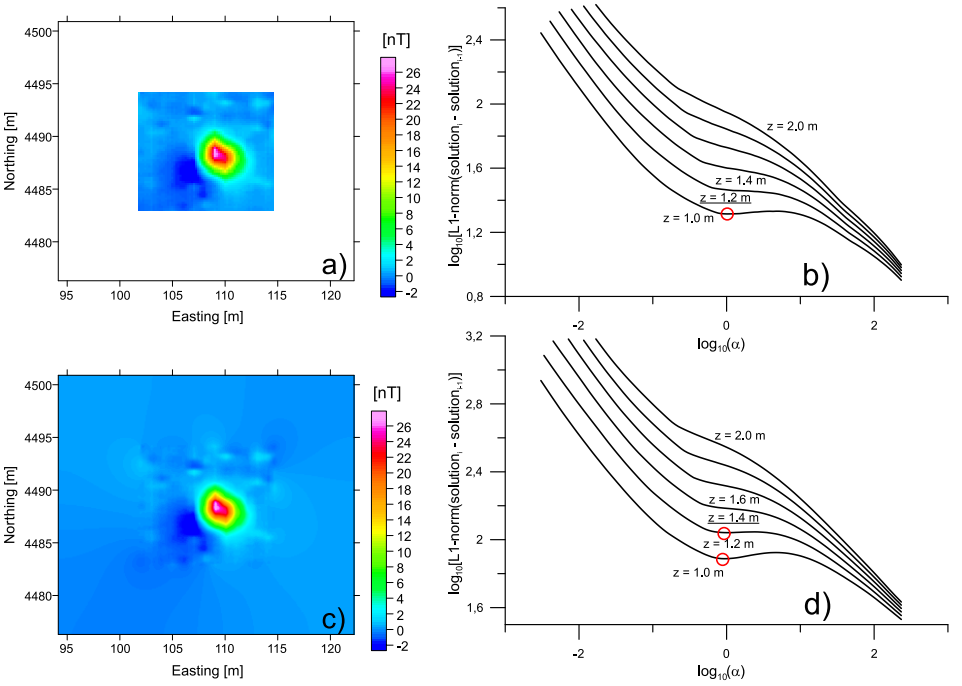

Fig. 11. Real world magnetic data-set, anomalous ΔT field over a 100 mm tank projectile, in the depth 1.9 m below the sensor: a) extracted measured data on 16×15 m area, b) corresponding L_1-norms, c) extrapolated data to 24×23 m area, d) corresponding L_1-norms. Sampling steps for all cases: $\Delta x = \Delta y = 0.1$ m.

tive shooting area in Rohožník-Studienka in SW Slovakia (survey was done because of planned vibroseismic survey in this area). As it was mentioned in the begin of this sub-chapter, magnetic data have been acquired in a net of 1.0×0.1 m points. One typical anomaly was selected for TRDC depth-estimation (Fig. 11a). This anomaly is connected with an unexploded 100 mm tank gun projectile, which was excavated in the depth 1.3 m below the surface (the average height of the magnetometer sensor over the earth surface was around 0.6 m). On the shapes of interpreted L_1-norms (Fig. 11b) it can be seen that the detected local minimum vanishes too early and the estimated source depth 0.6 m is too shallow (0.6 m = 1.2 m – 0.6 m). In this case unfortunately, the extrapolation by means of the mentioned partial differential equations together with sparse linear algebra approach (*D'Errico, 2012*) did not helped much. Estimated depth in the case of extrapolated grid (Fig. 11c) is slightly larger (Fig. 11d), but its value 0.8 m (1.4 m – 0.6 m) is in a large error, when compared with the real depth of the projectile (1.3 m). Here we can see that sometimes even such kind of extrapolation does not help and we have still to work on this aspect of the method (searching for better extrapolation methods).

6. Conclusions

Presented results show that during application of stable downward continuation methods (here the Tikhonov's regularization method was used) for the estimation of source depths also the discretization parameters of the interpreted fields can play an important role. The most important are the dimensions of the area covered by the interpreted field – in other words, there is a need for relatively large surroundings around the interpreted anomaly (from our experience these should be 5–10 times larger than the expected source depth). From this point of view, the method is more suitable for the interpretation of objects in near surface and mining geophysics (anomalies from cavities, UXO objects and ore bodies). Some extrapolation methods (based on partial differential equations approximation) can help in these situation. Beside of this, also the sampling step plays an important role – we can improve the properties of the method even by introduction of interpolated values, covering the area in a denser grid. Although, we do not

increase the information content of the anomalous field, but we improve the numerical aspects of the discrete Fourier transform evaluation, which is the basis of the method). From our experiences, at least 10 sampling points pro anomaly half-with should represent a material, which is good for the interpretation with this kind of methods. In this situations, the well know Kriging interpolation method gives the best results.

Together with this paper, we give a software solution of this proposed and analysed method – the Matlab script REGCONT2 is free for academic and scientific use and it can be downloaded together with supporting files and a user manual from the server: `http://www.kaeg.sk/vyskum/projekt-vega-2014/project-vega-1-0462-16/`.

Acknowledgements. Authors would like to express their thanks to Dr. Katarina Brazda from Vienna University and Dr. Peter Fiďo Richter for an inspiration in the derivation of basic spectral characteristics of the method, given in the paper Appendix. Thanks belong also to the company G-trend Ltd. Bratislava for allowing to publish the UXO magnetometric data from site Rohožník-Studienka. Published research was supported by the Slovak scientific agencies, projects VEGA 1/0141/15, VEGA 1/0462/16 and APVV-16-0146. Some aspects have been solved also a part of the scientific program in the project: Comenius University Science Park supported by the Research and Development Operational Programme funded by the ERDF Grant number ITMS 26240220086. Authors are thankful for valuable comments and suggestions, obtained in the frame of the review process.

References

Abedi M., Gholami A., Norouzi G. H., 2014: A new stable downward continuation of airborne magnetic data based on Wavelet deconvolution. Near Surface Geophysics **12**, 751–762.

Bath M., 1968: Mathematical aspects of seismology. Elsevier, 428 p.

Baranov W., 1975: Potential fields and their transformation in applied geophysics. Gebruder Borntraeger, Berlin-Stuttgart, 151 p.

Blakely R. J., 1995: Potential Theory in Gravity and Magnetic Applications. Cambridge University Press, UK, 441 p.

Cooper G., 2004: The stable downward continuation of potential field data. Explor. Geoph., **35**, 4, 260–265.

Cressie N. A. C., 1991: Statistics for Spatial Data. John Wiley and Sons, Inc., New York, 900 p.

D'Errico J., 2012: Interpolation (& extrapolation) of NaN elements in a 2d array – inpaint_nans Matlab function. (`https://de.mathworks.com/matlabcentral/fileexchange/4551-inpaint_nans`), MATLAB Central File Exchange. Retrieved October 10, 2017.

Elysseieva I. S., Pašteka R., 2009: Direct interpretation of 2D potential fields for deep structures by means of the quasi-singular points method. Geophysical Prospecting, **57**,4, 683–705.

Fedi M., Florio G., 2002: A stable downward continuation by using the ISVD method. Geophysical Journal International **151**, 146–156.

Florio G., Fedi M., 2018: Depth estimation from downward continuation: An entropy-based approach to normalized full gradient. Geophysics **83**, 3, J33-J42.

Glasko V. B., Litvinenko O. K., Melikhov V. R.,1970: Possibilities of regularizing algorithms for continuation of potential functions close to source masses. Prikladnaya Geofizika (Applied Geophysics) **60**, 142–157 (in Russian).

Hansen P. C., 2007: Regularization Tools Version 4.0 for Matlab 7.3. Numerical Algorithms **46**, 189–194.

Lawson C. L., Hanson R. J., 1974: Solving Least Squares Problems. Prentice-Hall, Englewood Cliffs, 305 p.

Li Y., Devriese S. G. R., Krahenbuhl R. A., Davis K., 2013: Enhancement of magnetic data by stable downward continuation for UXO application. IEEE Transactions on Geoscience and Remote Sensing, **51**, 6, 3605–3614.

Ma G., Liu C., Huang D., Li L., 2013: A stable iterative downward continuation of potential field data. Journal of Applied Geophysics **98**, 205–211.

Mudretsova E. A., Veselov K. E., Ed., 1990: Gravimetry. Nedra, Moscow, 607 p. (in Russian).

Pašteka R., Karcol R., Pašiaková M., Pánisová J., Kušnirák D., Beres J., 2011: Depth estimation of microgravity anomaliessources by means of regularized downward continuation and Euler deconvolution. 73rd EAGE Conference and Exhibition extended abstract, p. 1–5.

Pašteka R., Karcol R., Kušnirák D., Mojzeš A., 2012: REGCONT: A Matlab based program for stable downward continuation of geophysical potential fields using Tikhonov regularization. Computers and Geosciences, **49**, 278–289.

Smith W. H. F., Wessel P., 1990: Gridding with continuous curvature splines in tension. Geophysics, **55**, 3, 293–305.

Tikhonov A. N., Glasko V. B., Litvinenko O. K., Melichov V. P., 1968: Analytic continuation of a potential to disturbing masses by the regularization method. Izv., Earth Physics, **12**, 738–747.

Trompat H., Boschetti F., Hornby P., 2003: Improved downward continuation of potential field data. Exploration Geophysics **34**, 4, 249–256.

Troutman J. L., 1983: Variational Calculus with Elementary Convexity. Springer, 364 p.

Zeng X., Li X., Su J., Liu D., Zou H., 2013: An adaptive iterative method for downward continuation of potential-field data from a horizontal plane. Geophysics, **78**, 4, J43-J52.

Zeng X., Liu D., Li X., Chen D., Niu C., 2014: An improved regularized downward continuation of potential field data. Journal of Applied Geophysics, **106**, 114–118.

Zeng X., Li X., Jia W., Chen D., Liu D., 2015: Iterative Wiener filter for unstable linear transformations of potential field data. Journal of Applied Geophysics, **115**, 100–109.

Zhang H., Ravat D., Hu X., 2013: An improved and stable downward continuation of potential field data: The truncated Taylor series iterative downward continuation method. Geophysics, **78**, 5, J75-J86.

Zhang Y., Wong Y. S., Lin Y., 2016: BTTB-RRCG method for downward continuation of potential field data. Journal of Applied Geophysics, **126**, 74–86.

Zhang C., Lü Q., Yan J., Qi G., 2018: Numerical Solutions of the Mean-Value Theorem: New Methods for Downward Continuation of Potential Fields. Geophysical Research Letters, **45**, 8, 3461–3470.

Zhou S., Li J., Yuan Y., 2018: Downward Continuation of Potential Field Data Based on Chebyshev–Padé Approximation Function. Pure and Applied Geophysics, **175**, 1, 275–286.

Appendix

Derivation of the regularized downward continuation filter in Fourier domain

This derivation was inspired by the fundamental paper from *Tikhonov et al. (1968)* and we try to give it here with all needed details (for better understanding of the basic idea of regularization).

Based on the harmonic property of the continued potential field function U (potential or its higher derivative; which fulfils the Laplace's equation) and Green's third identity, the so-called Poisson's integral is valid for the analytical continuation (e.g. *Blakely, 1995, p. 316*):

$$U\left(x,y,z-\Delta z\right)=\frac{\Delta z}{2\pi}\int\limits_{-\infty}^{\infty}\int\limits_{-\infty}^{\infty}\frac{U\left(\xi,\eta,z\right)}{\left[\left(x-\xi\right)^{2}+\left(y-\eta\right)^{2}+\Delta z^{2}\right]^{3/2}}\,\mathrm{d}\xi\mathrm{d}\eta\,, \qquad \text{(A.1)}$$

(3D problem)

where $U(x,y,z-\Delta z)$ is the potential field on a depth level $h-\Delta z$ (further from the sources), $U(x,y,z)$ is the field on the level z (closer to the sources), Δz is the vertical continuation distance ($\Delta z>0$; z-axis is pointing downwards) and ξ, η are the equivalents of variables x, y in the integration plane. When the function $U(x,y,z-\Delta z)$ is searched then we speak about

an upward and when $U(\xi, \eta, z)$ inside the integral then about a downward continuation, respectively. Upward continuation is a stable operation (it is an integral transformation) and downward continuation is an unstable operation (it must be searched as a solution of an integral equation).

In the case of a 2D problem we can write:

$$U\left(x, z-\Delta z\right) = \frac{\Delta z}{\pi} \int\limits_{-\infty}^{\infty} \frac{U\left(\xi, z\right)}{\left[\left(x-\xi\right)^2 + \Delta z^2\right]} \mathrm{d}\xi \,. \qquad \text{(2D problem)} \qquad \text{(A.2)}$$

Equation (A.2) (and A.1 of course too) can be seen as a convolution integral: e.g. for the 2D problem it can be rewritten as $U(x, y, z-\Delta z) = U(x, z) \otimes K(x)$, where $\otimes$ is the convolution symbol and $K(x) = (1/\pi)((\Delta z/(x^2 + \Delta z^2))$ is the integral kernel function from (A.2). Convolution operation can be performed effectively in the Fourier domain using the convolution theorem, what will be used later on.

The most important aspect of the regularized solution creation in the sense of Tikhonov approach (*Tikhonov et al., 1968; Tikhonov and Arsenin 1977*) can be defined as a minimization problem solution – we have to minimize a functional (F), which is composed by two partial functionals (objective functions). The first of them is describing the closeness of the searched regularized solution to classical one (the searched function is continued upwards and compared with the original measured function); the second one is the regularizing (smoothing) functional, assuming the fact that a sum of the squared horizontal derivative of the searched solution should be as small as possible. The aim is to find a solution, which will be in a kind of "equilibrium" between these two conditions.

In the next part of the text we will derive, based on this minimization scheme, the solution for the downward continuation (*Tikhonov et al., 1968*). Because of the lack of simplicity we will derive it for the 2D problem, taking the starting level at $z = 0$, $U_0 = U(x, 0)$ and the downward continuation will be performed to the depth level $h(\Delta z = h)$, $y(x) = U(x, h)$. The minimization problem can be formulated as:

$$\int\limits_{-\infty}^{\infty} F[y, y', x] \mathrm{d}x = \int\limits_{-\infty}^{\infty} \left\{ \left[y \otimes K\left(x\right) - U_0\left(x\right) \right]^2 + \alpha \left[y'\left(x\right) \right]^2 \right\} \mathrm{d}x = \min. \,, \qquad \text{(A.3)}$$

where $y'(x)$ stands for the horizontal derivative of y with respect to $x(\partial y/\partial x)$ and α is the regularization parameter "managing" the influence of the second (stabilizing) functional upon the whole solution (physical unit of α is m^{-1}).

The aim of the solution of this minimization problem is to find the solution $y(x)$, for which the functional $F[\,]$ reaches a minimum. We use the known Euler-Lagrange equation from the variational calculus theory (e.g. *Bath, 1968; Troutman, 1983*) for finding an extreme of the variational problem:

$$\frac{\partial F}{\partial y} - \frac{\mathrm{d}}{\mathrm{d}x}\left[\frac{\partial F}{\partial y'}\right] = 0\,, \tag{A.4}$$

The first term of the Euler-Lagrange equation (A.4) is:

$$\frac{\partial F}{\partial y} = 2\,(y \otimes K - U_0)\,\frac{\partial\,(y \otimes K)}{\partial y} = 2\,(y \otimes K - U_0) \int\limits_{-\infty}^{+\infty} K\,(x-\xi)\,\mathrm{d}\xi =$$

$$= 2\,(y \otimes K - U_0)\,\frac{1}{\pi}\int\limits_{-\infty}^{+\infty} \frac{h}{(x-\xi)^2 + h^2}\mathrm{d}\xi = 2\,(y \otimes K - U_0)\,,$$

where the incident integral of the shifted kernel function is equal to 1 (with assumption $h > 0$).

The second term of the Lagrange-Euler equation (A.4) is:

$$\frac{\mathrm{d}}{\mathrm{d}x}\left[\frac{\partial F}{\partial y'}\right] = \frac{\mathrm{d}}{\mathrm{d}x}[2\alpha y'] = 2\alpha y''\,.$$

These results are substituted to equation (A.4) and we yield:

$$2y \otimes K - 2U_0 - 2\alpha y''\,. \tag{A.5}$$

This equation is solved in spectral domain by using theorems of spectrum of convolution and theorem of spectrum of differentiation of a function:
The Fourier transformations F of single terms are (u is the wave-number):

$F\{K(x)\} = \mathrm{e}^{-|u|h}$ – spectral characteristics of upward continuation ($h > 0$),
$F\{y(x)\} = \tilde{y}(\mathbf{u})$ – spectrum of the solution (regularized downward continued field),

$F\{y''(x)\} = -u^2\tilde{y}(u)$ – spectral characteristic of second horizontal derivative of the solution,
$F\{U_0(x)\} = \tilde{U}_0(u)$ – spectrum of measured field on the level $z = 0$.

Substituting these terms into the equation (A.5) gives (divided by factor 2):

$$\mathrm{e}^{-|u|h}\tilde{y} - \tilde{U}_0 - \alpha(-u^2)\tilde{y} = 0,$$

$$\tilde{y}\left[\mathrm{e}^{-|u|h} + \alpha u^2\right] = \tilde{U}_0,$$

$$\tilde{y}\left[1 + \alpha u^2 \mathrm{e}^{|u|h}\right] = \mathrm{e}^{|u|h}\tilde{U}_0.$$

The spectrum of searched solution is then equal:

$$\tilde{y} = \frac{1}{1 + \alpha u^2 \mathrm{e}^{|u|h}} \mathrm{e}^{|u|h}\tilde{U}_0, \tag{A.6}$$

where the first part (fraction) is a low-pass filter – the regularization term (controlled by the regularization parameter α), the second one $\exp(|u|h)$ is the spectral characteristics of the classical downward continuation and the third is the spectrum $\tilde{U}_0(u)$ of continued function $U_0(x)$. A part of the regularized solution is the search for an optimum value of the regularization parameter α (there exist several methods, in this paper we use the concept of C-norms, or in general $\mathrm{L_P}$-norms).

sciendo

Contributions to Geophysics and Geodesy Vol. 48/3, 2018 (255–269)

The deepest Moho in the Western Carpathians and its respective crustal density model (CEL12 section)

Dominika GODOVÁ[1], Miroslav BIELIK[1,2], Barbora ŠIMONOVÁ[1]

[1] Department of Applied and Environmental Geophysics,
Faculty of Natural Sciences, Comenius University,
Mlynská dolina, Ilkovičova 6, 842 48 Bratislava, Slovak Republic;
e-mail: bielik@fns.uniba.sk

[2] Earth Science Institute, Slovak Academy of Sciences,
Dúbravská cesta 9, P. O. Box 106, 840 05 Bratislava, Slovak Republic;
e-mail: geofmiro@gmail.com

Abstract: The main aim of this study is to compile 2-D density model of the CELEBRATION 2000 profile CEL12, which is based on seismic refraction data. The profile CEL12 crosses the External Western Carpathians Flysch zone and is located in the southern part of Poland. The general feature of the resultant density model shows significant changes in the crustal thickness. The Moho depth changes in the interval from 31 km to 43 km. The interpreted 43 km crustal thickness over a 60 km section of the profile results in the discovery of an area, which represents the thickest crust in the entire West Carpathians. This area is situated ∼50 km north-east from the High Tatras in Poland.

Key words: gravimetry, density modelling, seismic constraints, External Western Carpathians Flysch zone, CELEBRATION, Bouguer gravity

1. Introduction

The deep seated structure and dynamics of the Earth's lithosphere is one of the worldwide current research topics. The use of geophysical methods gives us advantage to expand our knowledge. Particularly seismics is one of the most used and most useful methods to describe the structure and composition of the Earth's crust. In last decades, many international projects, such as POLONAISE'97, CELEBRATION 2000, ALPS 2002 and SUDETES 2003 took place in the Central European region and contributed to very high level of survey coverage in this area (e.g. *Guterch et al., 2003a;*

doi: 10.2478/congeo-2018-0011

Grad et al., 2006; Środa et al., 2006; Hrubcová et al., 2005; 2010; Behm et al., 2007; Brückl et al., 2010; Brückl, 2011; Janik et al., 2011; Malinowski et al., 2009, 2013).

For research in the Western Carpathians and their immediate surroundings, the CELEBRATION 2000 (**C**entral **E**uropean **L**ithospheric **E**xperiment **B**ased on **R**efr**action 2000**) project was the most important. The project was held by 28 European and North American research institutions and contained 16 seismic refraction profiles crossing the ALCAPA region (*Guterch et al., 2003a,b*). These profiles were focused to cover the most of the tectonic units in Central Europe, such as the East European Craton, the Trans European Suture Zone (TESZ), the Western Carpathians, the Pannonian Basin, the Bohemian Massif and the Eastern Alps.

Further information on the crustal and lithospheric structure of Europe have been published by *Tesauro et al. (2008), Kaban et al. (2010), Jones et al. (2010), Plomerová and Babuška (2010), Zeyen et al. (2002), Dérerová et al. (2006), Grinč et al. (2013).* Important knowledge about the depths of Moho and lithosphere-asthenosphere boundary (LAB) have also been obtained by integrative 3-D modelling (LitMod) combining in a self-consistent manner concepts and data from thermodynamics, mineral physics, geochemistry, petrology and solid Earth geophysics (*Alasonati Tašárová et al., 2009, 2016*).

With its length of nearly 200 km, the seismic refraction profile CEL12 is one of the shortest profiles of the project CELEBRATION 2000. Located in the southern part of Poland (Fig. 1), it crosses exclusively the tectonic unit of the External Western Carpathians Flysch zone (Fig. 2). Despite of its short length, the main importance of this profile dwells in the fact that it crosses some of the other important CELEBRATION 2000 profiles. It contributes to result switchover between those profiles and broadens interpretation possibilities of the lithospheric structure in the Western Carpathians. The importance of the CEL12 profile lies above all in the discovery of the deepest Moho discontinuity (the thickest crust) in the Western Carpathian region.

The main aim of this study is to compile and interpret a 2-D density model along the seismic profile CEL12 based on the seismic refraction profiling results and other geophysical and geological constraining information.

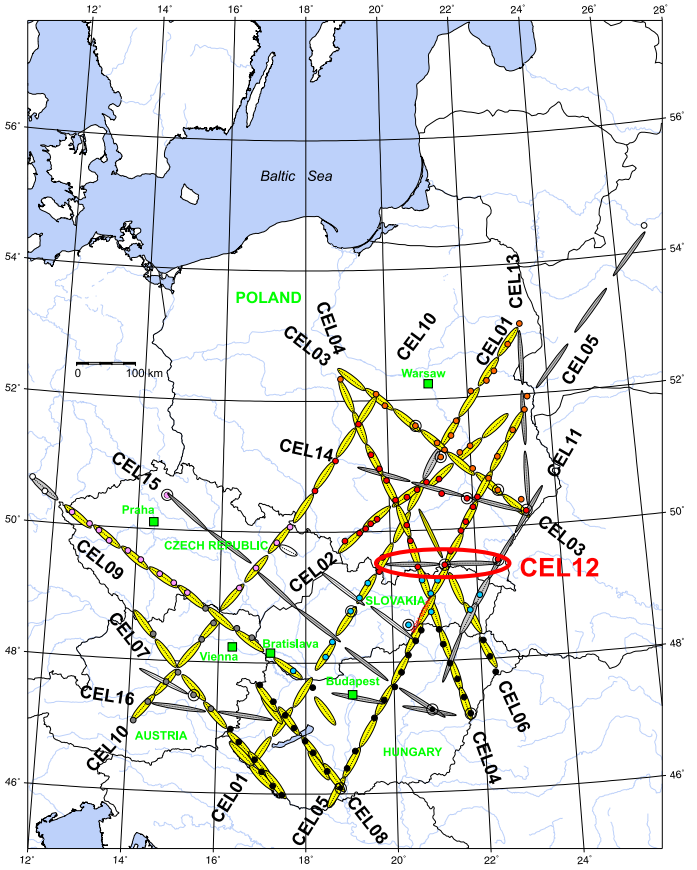

Fig. 1. Map of the CELEBRATION 2000 profiles (modified after *Guterch et al., 2003a*). The CEL12 profile is shown in red ellipse. The red, pink, blue, black, orange and grey color circles show shot points. Yellow lines are high density recording profiles, the other lines are low density recording profiles.

2. Geological setting

The CELEBRATION 2000 project crossed the Carpathian-Pannonian region, which is part of the ALCAPA microplate (including also the Transdanubic Range and the Eastern Alps). This area is subject to discussions regarding its structure and tectonic evolution (*Janik et al., 2011*). There are two main views about its Tertiary evolution. The first one suggests

the gravitational collapse of the continental lithosphere (e.g., *Knapp et al., 2005; Gemmer and Houseman, 2007*). The second one regards as crucial the process of subduction of the oceanic lithosphere, which is more accepted for its geological and geophysical evidence (e.g., *Csontos et al, 1992; Nemčok et al., 1998; Konečný et al., 2002; Alasonati Tašárová et al., 2009*).

The Western Carpathians are a mountain range with dominant nappe structure and characteristic north-vergent orogenetic processes migration

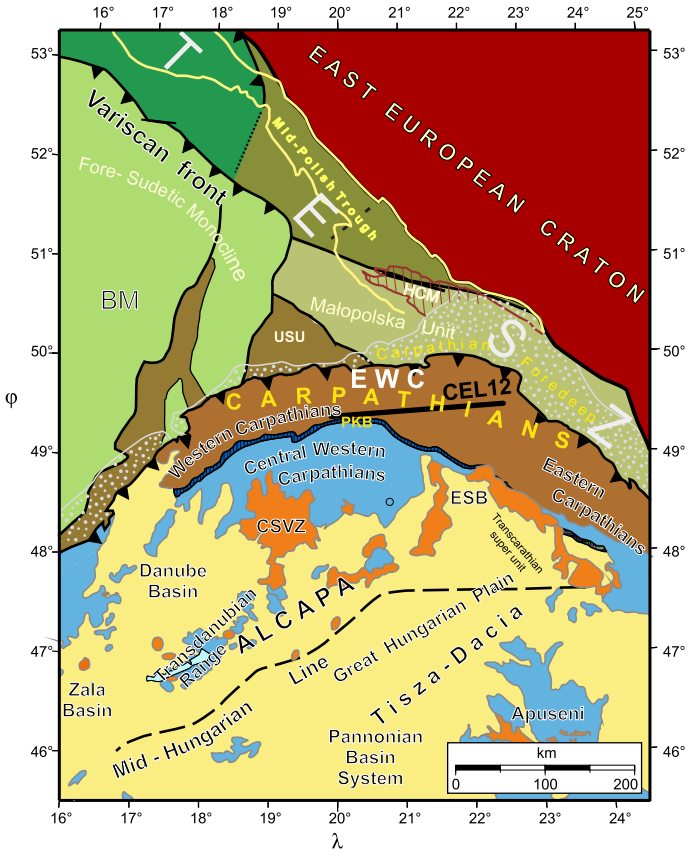

Fig. 2. Position of the CEL12 seismic profile on geological map of the Central Europe (modified after *Janik et al., 2011*). EWC – External Western Carpathians; HCM – Holy Cross Mts.; BM – Bohemian Massif; USU – Upper Silesian Unit; CSVZ – Central Slovak Volcanic zone; ESB – East Slovakian Basin; PKB – Pieniny Klippen Belt; TESZ – Trans-European Suture Zone.

(*Alasonati Tašárová et al., 2009*). The mountain range is circumscribed by the edge of alpine nappes in the north, Eastern Alps in the west, Uzh river valley in the east, while the southern boundary is poorly demarcated due to sedimentary cover of the Western Carpathian units (*Hók et al., 2001, 2014*). The Western Carpathians can be divided into the Internal Western Carpathians and External Western Carpathians (*Mišík et al., 1985*).

The seismic profile CEL12 is exclusively located in the External Western Carpathians (Fig. 2), which are separated from the Internal Western Carpathians by Pieniny Klippen Belt in the south (*Oszczypko et al., 2015*). The External Western Carpathians form a huge accretionary wedge with north-vergent nappe structure (*Środa et al., 2006; Hók et al., 2014*) composed of Cretaceous and Paleogene formations (*Oszczypko, 2004*). The basement is formed by the Epivariscan Platform with the thickness in range from hundreds to thousands meters beneath the Western Carpathians (*Oszczypko, 2004*). The Flysch zone has a typical development with the alternation of abyssal turbidity sediments (*Kováč et al., 2016*), more precisely shales and sandstones developing on the continental margins with thickness of sediments up to 18 km in the easternmost part (*Rylko and Tomaś, 2005; Janik et al., 2011*). The foreland was befallen by the subduction of the oceanic crust and lead to dying out of the basin of deposition from Upper Paleogene to Upper Miocene (*Alasonati Tašárová et al., 2009*) and successive detachment of the sediments and their accumulation as the accretionary wedge (*Hók et al., 2001*). The termination of the Magura Ocean lead to development of the anoxic setting and sedimentation of black shales. In the remains of the Magura Ocean, the Magura Basin was the exception with sedimentation of the syntectonic sandstones (e.g., *Kováč et al., 2016*).

3. Methodology

Quantitative interpretation of the gravity field along the seismic refraction profile CEL12 was compiled in 2-D density modelling software GM-SYS (Gravity and Magnetics Modelling system) created by Northwest Geophysical Associates, Inc. (NGA). The software was designed to calculate a gravity and/or magnetic response of the geological model, which offers user-friendly interface for interactive and intuitive creation and editing of geophysical

models based on observed gravity and/or magnetic data. The possibility to make the process of interpretation and testing alternate admissible solution faster is due to immediate calculation of the gravity and magnetic response of the model. It is possible to interactively manipulate the geometry and change density values for every block used in a model. The software also offers various features, such as $2^{3/4}$-D modelling, Extended Model Size, Gravity/Magnetic Gradients, Joint Inversion/Optimalization, Seismic Bitmap (*GM-SYS User's Guide for version 4.9, 2004*).

GM-SYS software uses a 2-D model of the Earth, which only changes in depth (axis Z) and along the direction of the profile (axis X) with the possibility to extend the model to "infinity" (±30 000 km) thus the 2-D model represents a complex of polygons extended to infinity in the direction of axis Y (*GM-SYS User's Guide for version 4.9, 2004*). This allows approximating various types of geological objects, such as faults, dikes and 3-D bodies extended in the direction of axis Y (*Csicsay, 2010*).

Gravity and magnetic response calculation of such bodies is based on methods by *Talwani et al. (1959)* and *Talwani and Heirtzler (1964)* with algorithm after *Won and Bevis (1987)*. $2^{1/2}$-D calculation is based on formula by *Rasmussen and Pedersen (1979)*. Methods patented by NGA were used to increase effectivity and speed of calculations and to better optimise the interactive interface. GM-SYS inversion implements the Marqardt inverse algorithm (*Marqardt, 1963*) and its application to gravimetry and magnetics was introduced by U.S. Geological Survey.

4. Input data

Gravity data, the key data type for creating a 2-D density model, were compiled from the gravity map of the southern part of Poland (*Królikowski and Petecki, 1995; Bielik et al., 2006*). Complete Bouguer Anomaly attains here values from –46.8 to –72.1 mGal (1 mGal = 10^{-5} ms^{-2}). At the beginning of the profile, there is an increasing trend of values from the initial –68 mGal up to –50 mGal at the 110 km distance. The highest values (more than –50 mGal) are at about the centre of the profile (111-th to 140-th km from the beginning of the profile), followed by rapid decrease of values towards the end of the profile, with values of about –68.5 mGal and less, which are

the lowest on the CEL12 profile.

Heights of the topographic suface were taken from GTOPO30 (*Gesch et al., 1999*) for 192 km long profile with a step of 1 km. Since our model is 2-D, it is important for the assessment of the results (*Zeyen et al. 2002*) to have some measure of the 3D variability of the input data. For this reason, we show the topography in Figures 3 and 4 not only along the profile CEL12 but in a stripe of 25 km width to both sides of the profile for topography. Higher topography is located in the western part of the profile with the highest value of 850 m above sea level (around 10-th km). The lowest point of the profile is 350 m above sea level (∼120-th km).

Comparing the gravity and topography (Fig. 3) we can say that there is a good (negative) correlation between them. Generally, the higher topography correlates with lower values of the Complete Bouguer Anomalies. This fact can indicate a compensation of topography in depth, e.g. by the Moho discontinuity (*Bielik, 2000*). And vice-versa, the section with the lowest topography has the highest observed gravity values, which can indicate the elevation of Moho. However, this assumption may not be applicable everywhere.

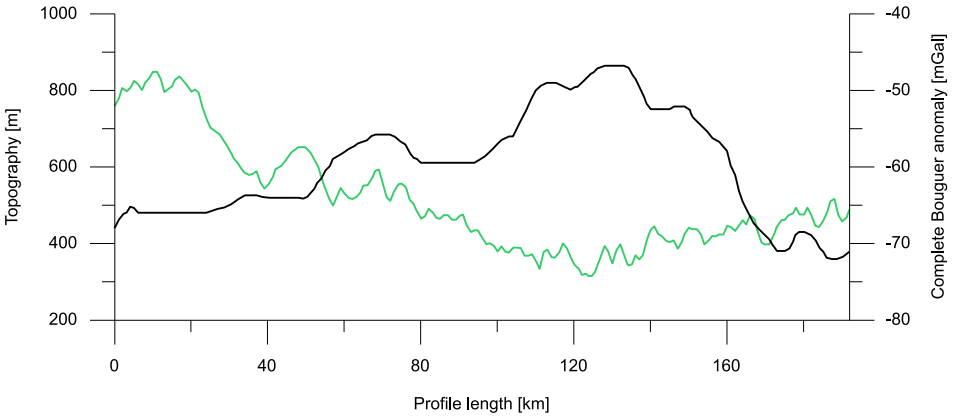

Fig. 3. Graph comparing the gravity (black line) and topography (green line) data.

The CEL12 seismic refraction profile (Fig. 4) compiled by *Janik et al. (2011)* was used to define input data regarding geometry and position of density anomalous bodies, which are approximated by polygons in the GM-SYS software. The length of this profile is 192 km and its vertical section

extends down to 80 km in depth. The longitudinal seismic wave velocities v_p change between 2.73 and 8.38 km s^{-1}. *Janik et al. (2011)* divided the cross-section into several layers according to these velocities. The uppermost layer, represented by velocities up to $v_p = 4.90$ km s^{-1}, corresponds to the sedimentary layer, the thickness of which varies from 2 to 8 km. The velocities between $v_p = 4.90$ km s^{-1} and 6.10 km s^{-1} represent the upper part of the upper crust with thickness from 6 km in the western part of the profile to nearly 24 km in the central part. After interpretation by *Janik et al. (2011)*, the layer with velocities $v_p = 6.30 - 6.50$ km s^{-1} represents the lower part of the upper (Penninic) crust (in the western part of the profile it reaches 16 km thickness). The lower crust is represented by seismic velocities between 6.50 km s^{-1} and 6.83 km s^{-1}, but this range does not appear throughout the whole profile length. It is divided into two separate layers

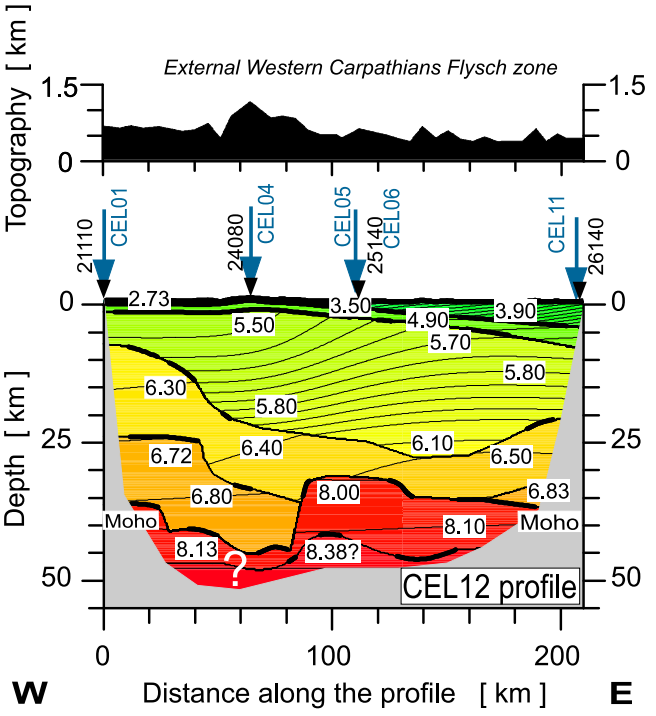

Fig. 4. The 2D model of seismic P-wave velocity in the crust and uppermost mantle along the CELEBRATION 2000 profile CEL12 compiled by *Janik et al. (2011)*. Blue arrows show the positions of the CELEBRATION 200 profiles crossing the CEL12 profile.

by the elevation of the Moho discontinuity in the central part of the profile. The uppermost part of the upper mantle is characterized by v_p from $8.00\,\mathrm{km\,s^{-1}}$ up to $8.38\,\mathrm{km\,s^{-1}}$. The Moho depression near the central part of the profile is represented by a depth of 43 km, which indicates the thickest crust in the Western Carpathians.

The required densities for the anomalous bodies along the profile CEL12 were obtained by transformation of P-wave velocities v_p to densities by formulas of Sobolev-Babeyko (*Sobolev and Babeyko, 1994*), Christensen-Mooney (*Christensen and Mooney, 1995*) and Lachenbruch-Morgan (*Lachenbruch and Morgan, 1990*). The last formula was used to determine the densities of the anomalous layers located within the lower lithosphere (*Šimonová and Bielik, 2016*). The calculated density values are for: the External Western Carpathians sedimentary layer 2.49–2.59 $\mathrm{g\,cm^{-3}}$; the upper crust 2.26–2.82 $\mathrm{g\,cm^{-3}}$ (after *Christensen and Mooney, 1995*, or 2.64–2.69 $\mathrm{g\,cm^{-3}}$ after *Sobolev and Babeyko, 1994*), with average of 2.61 $\mathrm{g\,cm^{-3}}$; the lower crust from 2.75 $\mathrm{g\,cm^{-3}}$ (or 2.76 $\mathrm{g\,cm^{-3}}$ after *Sobolev and Babeyko, 1994*) up to 3.01 $\mathrm{g\,cm^{-3}}$, with average value 2.89 $\mathrm{g\,cm^{-3}}$; the lower lithosphere from 3.34 to 3.38 $\mathrm{g\,cm^{-3}}$ (or 3.38 $\mathrm{g\,cm^{-3}}$ after *Lachenbruch and Morgan, 1990*), with average of 3.37 $\mathrm{g\,cm^{-3}}$ (*Šimonová and Bielik, 2016*).

5. Modelling results

On the basis of the data mentioned above we constructed an initial density model. The input parameters of the anomalous density bodies were modified by trial and error until a reasonable fit was obtained between observed gravity and calculated data (Fig. 5). The maximum average error along the profile was only ± 0.988 mGal, except for the beginning of the profile. These differences could be explained by a presence of near surface inhomogeneity. The final densities are shown in Fig. 5.

A general feature of the resultant density model is that the crustal thickness varies significantly along the profile CEL12. The Moho depth changes from 31 km to 42 km. The crustal thickness at the beginning of the profile is about 36 km, and to the east it gradually increases to a depth of 43 km (at 60-th km of profile). This thickness of the crust is the largest in the whole area of the Western Carpathians. At 75-th km of profile the Moho

boundary rises sharply to a depth of only 31 km and in the interval from 80-th to 110-th km of the section only insignificant Moho elevation can be observed. Next to the east, the crustal thickness increases when it reaches 38 km at the end of the profile. Note that the large changes of Moho depth can be observed in a relatively short interval (190 km) and in only a single tectonic unit – the External Western Carpathian Flysch zone. This is a significant finding.

The crust consists of four anomalous density layers: sedimentary, upper part of the upper crust, lower part of the upper crust and lower crust.

The sedimentary layer consists of two parts. The maximum thickness of the western part with 2.40 g cm^{-3} density reaches about 6 km and its thickness thins out significantly to the east. The eastern part of the sedimentary layer is characterized by thickness, which varies from 0 to 10 km.

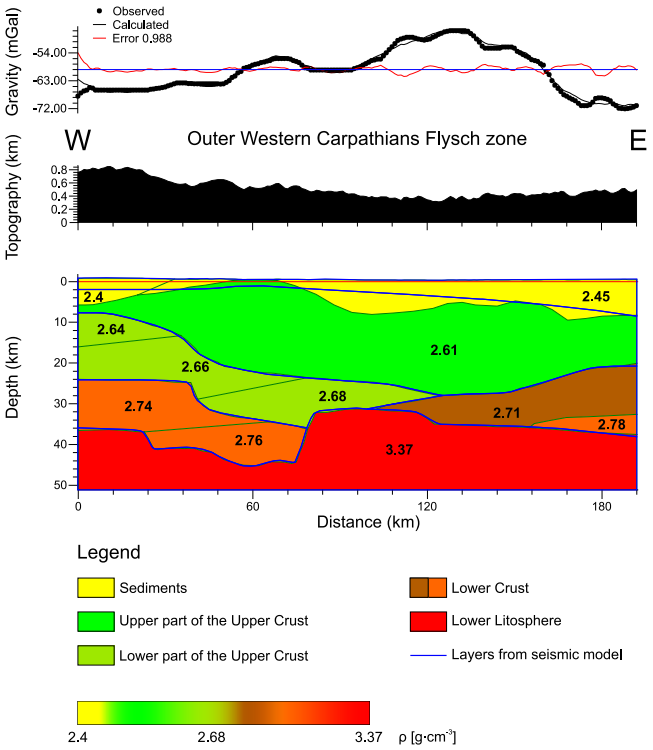

Fig. 5. 2-D density model of the profile CEL12. Blue lines show the seismic model used as a starting model.

The upper crust consists of two layers. The upper part of the upper crust is represented by lower average density 2.61 g cm^{-3} and its thickness varies from about 2 km up to 20 km. The lower part of the upper crust dips in the direction from west to east. In the same direction, its average density is also increasing from 2.64 g cm^{-3} to 2.68 g cm^{-3}. The depth of the boundary between them varies from 7.5 km (0-th km of the profile) up to 28 km (120-th km of the profile). The western part of the lower crust is represented by average density 2.74–2.76 g cm^{-3} and its thickness varies from 8 to 12 km. The upper boundary of this layer varies from 24 km up to 34 km. The eastern part of the lower crust has average density 2.71–2.78 g cm^{-3}. Its thickness at the end of the profile reaches 17 km, while towards the west this part of the lower crust thins out and at the 96-th km of the profile reaches thickness of 0 km.

The lower lithosphere (uppermost part of the upper mantle) is characterized by average density of 3.37 g cm^{-3}.

6. Discussion and Conclusion

The orientation of the profile CEL12 in terms of 2-D modelling is not ideal as it is nearly parallel to the course of the External Western Carpathian unit (Fig. 2). In spite of this, the agreement between the results of seismic and gravimetric modelling is excellent.

The results of 2-D density modelling confirmed the seismic interpretation along the profile CEL12, which has discovered that the crustal thickness over the profile interval from 24-th km to 72-nd km reaches more than 42 km. Based on the knowledge about the depth of the Moho discontinuity (e.g. *Janik et al., 2011; Bielik et al., 2018*), it is known that this crustal thickness is the largest in the whole area of the Western Carpathians.

The results of 2-D density modelling show clearly that significant changes can be expected in the thicknesses of the crust, sedimentary layer, upper and lower crust not only along and across the Western Carpathians but also within its individual tectonic units of which they are composed.

Acknowledgements. This work was supported by the Slovak Grant Agency VEGA, grants No. 1/0141/15, 2/0042/15, and APVV grants No. APVV-16-0146, APVV-16-0482.

References

Alasonati Tašárová Z., Afonso J. C., Bielik M., Götze H. J., Hók J., 2009: The lithospheric structure of the Western Carpathian-Pannonian Basin region based on the CELEBRATION 2000 seismic experiment and gravity modeling. Tectonophysics, **475**, 454–469.

Alasonati Tašárová Z., Fullea J., Bielik M., Środa P., 2016. Lithospheric structure of Central Europe: Puzzle pieces from Pannonian Basin to Trans-European Suture Zone resolved by geophysical-petrological modelling. Tectonics, **35**, 1–32, doi: 10.1002/2015TC003935.

Behm M., Brückl E., Mitterbauer U., 2007: A New Seismic Model of the Eastern Alps its Relevance for Geodesy and Geodynamics. VGI Österrreichische Zeitschrift für Vermessung & Geoinformation, **2**, 121–133.

Bielik, M., 2000: Study of the gravity field in the Tibetan Plateau. Contributions to Geophysics & Geodesy, **30**, 4, 343–358.

Bielik M., Kloska K., Meurers B., Švancara J., Wyberaniec S., Fancsik T., Grad M., Grand T., Guterch A., Katona M., Królikowski C., Mikuška J., Pašteka R., Petecki Z., Polechońska O., Ruess D., Szalaiová V., Šefara J., Vozár J., 2006: Gravity anomaly map of the CELEBRATION 2000 region. Geologica Carpathica, **57**, 3, 145–156.

Bielik M., Makarenko I., Csicsay K., Legostaeva O., Starostenko V., Savchenko A., Šimonová B., Dérerová J., Fojtková L., Pašteka R., Vozár J., 2018: The refined Moho depth map in the Carpathian-Pannonian region. Contributions to Geophysics and Geodesy, **47**, 2, 179–190, doi: 10.2478/congeo-2018-0007.

Brückl E., 2011: Lithospheric Structure and Tectonics of the Eastern Alps – Evidence from New Seismic Data. In: Tectonics, Ed.: Closson D. InTech, Available from: http://www.intechopen.com/books/tectonics/lithospheric-structure-and-tectonics-of-the-eastern-alps-evidence-from-new-seismic-data.

Brückl E., Behm M., Decker K., Grad M., Guterch A., Keller G. R., Thybo H., 2010: Crustal structure and active tectonics in the Eastern Alps. Tectonics, **29**, 1–17.

Christensen N. I., Mooney W. D., 1995: Seismic velocity structure and composition of the continental crust: A global view. Journal of Geophysical Research **100**, B7, 9761–9788.

Csicsay K., 2010: Two-dimensional and three-dimensional itegrated iterpretation of gravity field within the frame of international project CELEBRATION 2000. PhD. thesis, Faculty of Natural Sciences of Comenius University, Bratislava, 155 (in Slovak).

Csontos L., Nagymarosy A., Horváth F., Kováč M., 1992: Tertiary evolution of the Intra-Carpathian area: a model. Tectonophysics, **208**, 221–241.

Dérerová J., Zeyen H., Bielik M., Salman K., 2006. Application of integrated geophysical modeling for determination of the continental lithospheric thermal structure in the eastern Carpathians. Tectonics, **25**, 3, 1–12. TC3009, doi: 10.1029/2005TC001883.

Gemmer L., Houseman G. A., 2007: Convergence and extension driven by lithospheric gravitational instability: evolution of the Alpine-Carpathian-Pannonian system. Geophysical Journal International, **168**, 1276–1290.

Gesch D. B., Verdin K. L., Greenlee S. K., 1999: New land surface digital elevation model covers the Earth. Eos Trans. AGU, **80**, 69–70. [online] [cit. 2018-04-03]. Available from: https://www.ngdc.noaa.gov/mgg/topo/report/s7/s7Bi.html.

GM-SYS®, 2004: User's Guide for version 4.9. Northwest Geophysical Associates, Inc., Corvallis, 101.

Grad M., Guterch A., Keller G. R., Janik T., Hegedűs E., Vozár J., Slaczka A., Tiira T., Yliniemi J., 2006: Lithospheric structure beneath trans-Carpathian transect from Precambrian platform to Pannonian Basin: CELEBRATION 2000 seismic profile CEL05. J. Geophys. Res., **111**, 1–23.

Grinč M., Zeyen H., Bielik M., Plašienka D., 2013. Lithospheric structure in Central Europe: Integrated geophysical modeling, J. Geodyn., **66**, 13–24, doi: 10.1016/j.jog.2012.12.007.

Guterch A., Grad M., Špičák A., Brückl E., Hegedűs E., Keller G. R., Thybo H., CELEBRATION 2000, ALP 2002, SUDETES 2003 working groups 2003a: Special contributions: An overview of recent seismic refraction experiments in central Europe. Studia Geophysica et Geodaetica, **47**, 3, 659–669.

Guterch A., Grad M., Špičák A., Brückl E., Hegedűs E., Keller G. R., Thybo H., CELEBRATION 2000, ALP 2002, SUDETES 2003 working groups, 2003b: Special contributions: An overview of recent seismic refraction experiments in central Europe. Studia Geophysica et Geodaetica, **47**, 3, 651–657.

Hók J., Kahan Š., Aubrecht R., 2001: Geology of Slovakia. 1st ed., 34–36. (in Slovak), ISBN 80-223-1592-3.

Hók J., Šujan M., Šipka F., 2014: Tectonic division of the Western Carpathians: an overview and a new approach. Acta Geologica Slovaca, **6**, 2, 135–143.

Hrubcová P., Środa P., Špičák A., Guterch A., Grad M., Keller G. R., Brückl E., Thybo H., 2005: Crustal and uppermost mantle structure of the Bohemian Massif based on CELEBRATION 2000 data. J. Geophys. Res., **110**, 1–21.

Hrubcová P., Środa M., Grad M., 2010: From the Variscan to the Alpine Orogeny: crustal structure of the Bohemian Massif and the Western Carpathians in the light of the SUDETES 2003 seismic data. Geophysical Journal International, Geodynamics and tectonics, **183**, 2, 611–633, doi: 10.1111/j.1365-246X.2010.04766.x.

Janik T., Grad M., Guterch A., Vozár J., Bielik M., Vozárová A., Hegedűs E., Kovács C. A., Kovács I., CELEBRATION 2000 Working Group, 2011: Crustal structure of the Western Carpathians and Pan-nonian Basin System: seismic models from CELEBRATION 2000 data and geological implication. Journal of Geodynamics, **52**, 2, 97–113.

Jones A. G., Plomerová J., Korja T., Sodoudi F., Spakman W., 2010. Europe from the bottom up: A statistical examination of the central and northern European lithosphere-asthenosphere boundary from comparing seismological and electromagnetic observations. Lithos, **120**, 1–2, 14–29, doi: 10.1016/j.lithos.2010.07.013.

Kaban M. K., Tesauro M., Cloetingh S., 2010. An integrated gravity model for Europe's crust and upper mantle, Earth Planet. Sci. Lett., **296**, 195–209. doi: 10.1016/j.epsl.2010.04.041.

Knapp J. H., Knapp C. C., Raileanu V., Matenco L., Mocanu V., Dinu C., 2005: Crustal constraints on the origin of mantle seismicity in the Vrancea Zone, Romania: The case for active continental lithospheric delamination. Tectonophysics, **410**, 311–323.

Konečný V., Kováč M., Lexa J., Šefara J., 2002: Neogene evolution of the Carpatho-Pannonian region: an interplay of subduction and back-arc diapiric uprise in the mantle. European Geosciences Union, Stephan Mueller Special Publication Series, **1**, 105–123.

Kováč M., Plašienka D., Soták J., Vojtko R., Oszczypko N., Less G., Ćosović V., Fügenschuch B., Králiková S., 2016: Paleogene palaeogeography and basin evolution of the Western Carpathians, Northern Pannonian domain and adjoining areas. Global and Planetary Change, **140**, 9–27.

Królikowski C., Petecki Z., 1995: Gravimetric atlas of Poland. Państwowy Instytut Geologiczny, Warszawa.

Lachenbruch A. H., Morgan P., 1990: Continental extension, magmatism and elevation; formal relations and rules of thumb. Tectonophysics, **174**, 39–62.

Malinowski M., Guterch A., Narkiewicz M., Probulski J., Maksym A., Majdański M., Środa P., Czuba W., Gaczyński E., Grad M., Janik T., Jankowski L., Adamczyk A., 2013: Deep seismic reflection profile in Central Europe reveals complex pattern of Paleozoic and Alpine accretion at the East European Craton margin. Geophysical Research Letters, **40**, 1–6.

Malinowski M., Środa P., Grad M., Guterch A., CELEBRATION 2000 Working Group, 2009: Testing robust inversion strategies for three-dimensional Moho topography based on CELEBRATION 2000 data. Geophys. J. Int., **179**, 1093–1104.

Marqardt D. W., 1963: An algorithm for least squares estimation of non-linear parameters. Journal of the Society for Industrial and Applied Mathematics, **11**, 431–441.

Mišík M., Chlupáč I., Cicha I., 1985: Stratigraphic and historical geology. 1st ed., SPN Bratislava, 304–44 (in Slovak).

Nemčok M., Pospíšil L., Lexa J., Donelick R. A., 1998: Tertiary subduction and slab break-off model of the Carpathian-Pannonian region. Tectonophysics, **295**, 307–340.

Oszczypko N., 2004: The structural position and tectonosedimentary evolution of the Polish Outer Carpathian. Przeglad Geologiczny, **52**, 2, 65–82.

Oszczypko N., Ślaczka A., Oszczypko-Clowes A., Olszewska B. 2015: Where was the Magura Ocean. Acta Geologica Polonica, **65**, 3, 319–344.

Plomerová J., Babuška V., 2010: Long memory of mantle lithosphere fabric – European LAB constrained from seismic anisotropy. Lithos, **120**, 131–143.

Rasmussen R., Pedersen L. B., 1979: End corrections in potential field modeling. Geophysical Prospecting, **27**, 4, 749–760.

Ryłko W., Tomaś A., 2005: Basement structure below the West-Carpathian-East Carpathian orogen junction (eastern Poland, north-eastern Slovakia and western Ukraine). Geologica Carpathica, **56**, 1, 29–40.

Šimonová B., Bielik M., 2016: Determination of rock densities in the Carpathian-Pannonian Basin Litosphere: based on the CELEBRATION 2000 experiment. Contributions to Geophysics and Geodesy, **46**, 4, 269–287.

Sobolev S. V., Babeyko A. Y., 1994: Modeling of mineralogical composition, density and elastic wave velocities in anhydrous magmatic rocks. Surveys in Geophysics, **15**, 5, 515–544.

Środa P., Czuba W., Grad M., Gutterch A., Tokraski A. K., Janik T., Rauch M., Keller G. R., Hegedűs E., Vozár J., CELEBRATION 2000 Working Group, 2006: Crustal and upper mantle structure of the Western Carpathians from CELEBRATION 2000 profiles CEL01 and CEL04: seismic models and geological implications. Geophys. J. Int., **167**, 737–760.

Talwani M., Heirtzler J. R., 1964: Computation of magnetic anomalies caused by two-dimensional bodies of arbitrary shape. In: Parks G. A. (Ed.), Computers in the mineral industries, Part 1: Stanford Univ. Pub., Geological Sciences, **9**, 464–480.

Talwani M., Worzel J. L., Landisman M., 1959: Rapid gravity computations for two dimensional bodies with application to the Mendocino submarine fracture zone. Journal of Geophysical Research, **64**, 49–59.

Tesauro M., Kaban M. K., Cloetingh S., 2008. EuCRUST-07: A new reference model for the European crust. Geophys. Res. Lett., **35**, L05313, doi: 10.1029/2007GL032244.

Won I. J., Bevis M. G., 1987: Computing the gravitational and magnetic anomalies due to a polygon: Algorithms and Fortran subroutines. Geophysics, **52**, 232–238.

Zeyen H., Dérerová J., Bielik M., 2002. Determination of the continental lithosphere thermal structure in the Western Carpathians: integrated modelling of surface heat flow, gravity anomalies and topography. Physics of the Earth and Planetary Interiors, **134**, 89–104.

sciendo

Contributions to Geophysics and Geodesy Vol. 48/3, 2018 (271–279)

Surface displacements, deformations and gravity changes due to underground heat source

Ladislav BRIMICH, Igor KOHÚT

Earth Science Institute, Slovak Academy of Sciences,
Dúbravská cesta 9, P. O. Box 106, 840 05 Bratislava, Slovak Republic;
e-mail: Ladislav.Brimich@savba.sk

Abstract: Thermo-elastic strains and stresses play a considerable role in the stress state of the lithosphere and its dynamics, especially at pronounced positive geothermal anomalies. Topography has a significant effect on ground deformation. Two methods for including the topographic effects in the thermo-viscoelastic model are described. First we use an approximate methodology which assumes that the main effect of topography is due to the distance from the source to the free surface and permits to have an analytical solution very attractive for solving the inverse problem. A numerical solution (for 2D plain strain case) is also computed using finite element method (FEM). The numerical method allows to include the local shape of the topography in the modeling. In the numerical model the buried magmatic body is represented by a finite volume thermal source. The temperature distribution is computed by the higher-degree FEM. For analytical as well as numerical model solution only the forces of thermal origin are considered. The results show that for the volcanic areas with prominent topography, its effect on the perturbation of the thermo-viscoelastic solution (deformation and total gravity anomaly) can be quite significant. In consequence, neglecting the topography could give erroneous results in the estimated source parameters.

Key words: displacements, deformations, gravity changes

1. Introduction

A magma intrusion in the Earth's crust will cause effects (for example deformation and gravity changes) related to its mass as well to the pressurization of the chamber due to overfilling or temperature changes. The theory of the thermoelastic phenomena shows that thermo-elastic stresses and deformations can arise in an elastic continuum if an inhomogeneous temperature

doi: 10.2478/congeo-2018-0012

field exists in the media (see e.g., *Nowacki, 1962*). Thus we can expect various thermoelastic phenomena to occur in some regions like volcanic areas, with an anomalous behaviour of the heat flow. In the geodynamic theory, it is well-known that thermo-elastic strains and stresses play a considerable role in the stress state of the lithosphere and its dynamics, especially in localities with pronounced geothermal anomalies (*Combs and Hadley, 1977; Teisseyre, 1986*). Therefore, *Hvoždara and Rosa (1979, 1980)* carried out a theoretical analysis of thermo-elastic deformations of a homogeneous half-space due to a point or linear source of heat, located at a particular depth in the half-space. They proved that thermo-elastic stresses are of expansive type and that they considerably disturb the normal lithostatic stress, specially near the surface of the half-space. *Hvoždara and Brimich (1991)* presented basic formulae and the results of numerical calculations for the simplified mathematical models of two important effects due to magmatic bodies in the Earth's lithosphere: a) static thermoelastic deformations, b) static elastic deformations due to upward pressure. The magmatic body is approximated by a finite volume source of heat in the first model and by a concentrated vertical force in the second one. The formulae for gravity anomaly due to non-uniform extension connected with thermo-elastic deformations were derived in *Hvoždara and Brimich (1995)*.

Many of the models with inelastic properties considered so far are analytical. They assume point source of deformation and a flat, horizontal free surface. Volcanoes are commonly associated with significant topographic relief. The approximation of Earth's surface as flat and use half-space solutions can lead to erroneous interpretation of the deformation data (see e.g., *Cayol and Cornet, 1998; Williams and Wadge, 1998, 2000; Folch et al., 2000*). *Williams and Wadge, (1998, 2000)* and *Cayol and Cornet (1998)* pointed out that topography has a significant effect on predicted surface deformation by elastic models in regions of significant relief. According to those studies the interpretation of ground-surface displacements with half-space models can lead to erroneous estimations. *Cayol and Cornet (1998)* found that the steeper the volcano, the flatter the vertical displacement field. *Folch et al. (2000)* demonstrated that this result is dramatically emphasised in the viscoelastic case, where the topography changes substantially both the magnitude and the pattern of the displacement field. They also showed that neglecting the topographic effects may, in some cases, introduce an

error greater than the one implicit in the point source hypothesis. Those reasons led us to study the effect of topography on surface displacements and gravity changes.

2. Analytical solution

The thermo-visco-elastic model presented in *Hvoždara (1992)* was applied to estimate the volcanic ground deformations. Fundamental equations for the uncoupled thermo-visco-elastic problem for a point heat source located at depth ζ are given in *Nowacki (1962)*. Thermo-visco-elastic gravity anomaly on the surface is given by *Brimich (2000)*.

Charco et al. (2002) propose a simple method for including topographic effects in a 3D thermo-visco-elastic model that allows the source depth to vary with the relief. On the Fig. 1 is the sketch of the model used in the analytical approach. The Figs 2, 3 and 4 show horizontal, vertical thermo-viscoelastic displacement (in m) as well as the gravity changes computed for different relaxation times and the static value (thermoelastic case) considering (a) a flat surface, and (b)–(d) axially-symmetric volcanic cone with an average slope of the flanks of 15°, 20° and 30° respectively. The influence of the topography is visible as the horizontal shift of maximal values of the both displacement components and particularly the gravity changes.

The simple method for evaluating the topographic effect in three-dimensional deformation model is based on the assumption, that the main effect

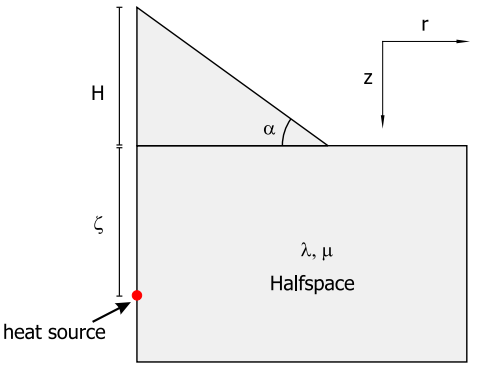

Fig. 1. Sketch of the model used in the analytical approach.

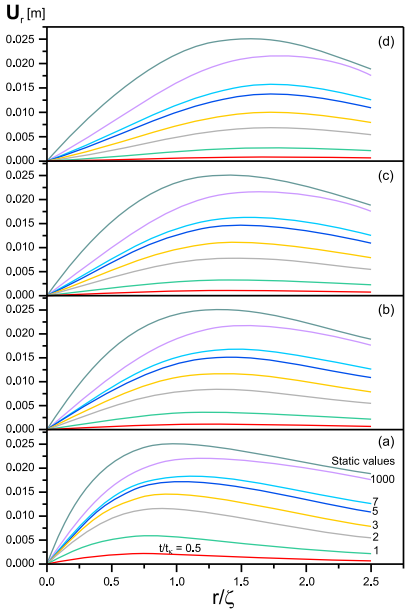

Fig. 2. Radial displacements.

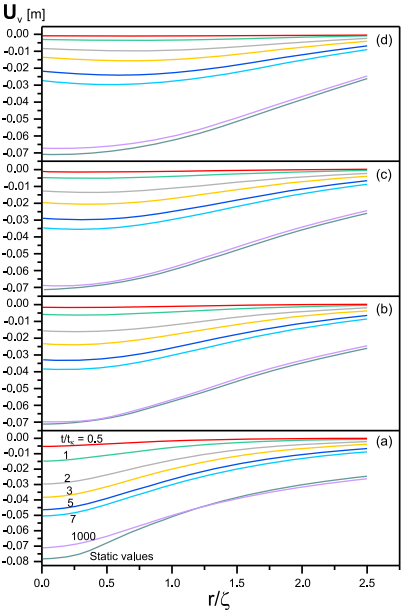

Fig. 3. Vertical displacements.

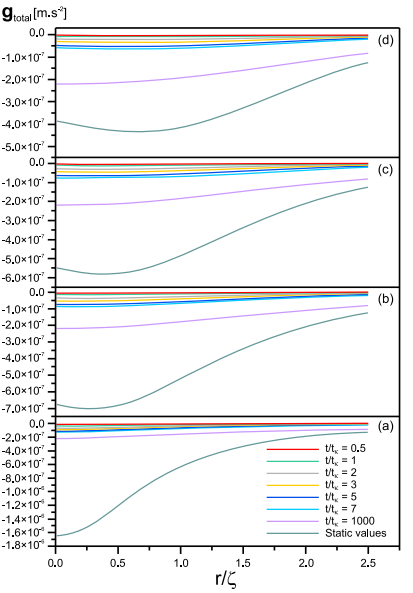

Fig. 4. Gravity changes.

of the topography is due to the distance from the heat source to the free surface. The solution on the surface is achieved by the consecutive computation of the source influence with corresponding depth of the heat source for the each point. The varying depth methodology was introduced by *Williams and Wadge (2000).*

3. Numerical solution

To include the topography effect in the thermoelastic solution we have used the finite element method computation. The principles and basics of finite-element method are generally known and are described in numerous monographs (e.g. *Irons and Ahmad, 1986; Babuška and Szabo, 1990*). All the computations were performed by the COMSOL Multiphysics© software. Although numerical methods are time consuming, they can handle models with realistic geometry.

The models are homogeneous, isotropic, axially-symmetric with respect to vertical axis. The vertical axis of symmetry is passing through the heat source. Two model versions have been computed – with and without topographical feature modeling the volcano cone (of 2 km height). The summit of the volcano is located over the thermal source. The domain's horizontal length is 120 km and the vertical span is from +2 to –38 km in order to minimize the influence of the external boundaries. The heat source is modeled by the spherical body in the depth of 5 km. In the computation only the forces of thermal origin are considered.

In the first step, the domain was divided into finite elements. The mesh corresponding to each plane section is formed by 19568 triangular elements. In the neighborhood of the thermal source, the mesh is refined into smaller elements due to the large gradients of computed fields in this area (see Fig. 5). On the Figs. 6 and 7 the radial and vertical displacements obtained by FEM are given.

The finite element method can model more complex models with sources of different geometries and elastic properties of the medium varying with depth. While the analytical approximate methodology can be very attractive for solving the inverse problem, the numerical method described above may be used to include the topography in a more realistic model that permits the consideration of non-uniform elastic and thermal properties of the

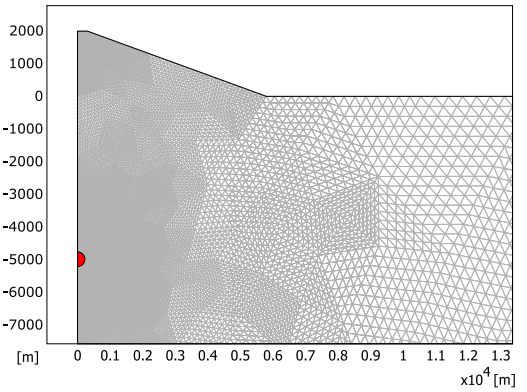

Fig. 5. Mesh with the position of the heat source.

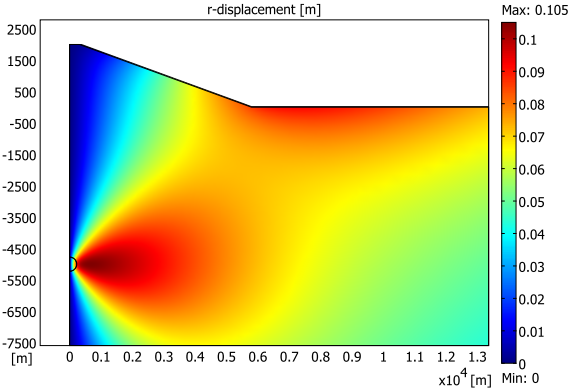

Fig. 6. Radial displacements.

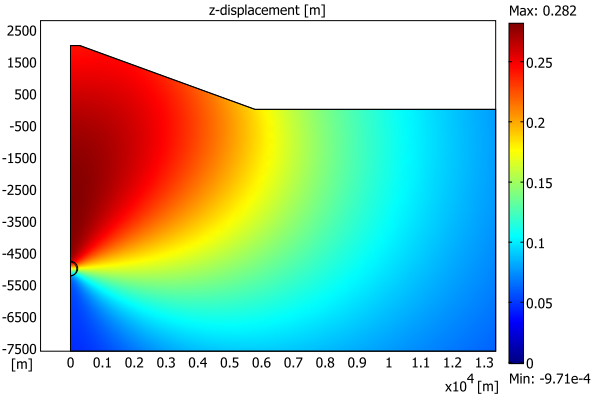

Fig. 7. Vertical displacements.

medium and the true shape of the Earth's surface. The comparison of the horizontal and vertical displacements for the different models in the Figs. 8 and 9 are given.

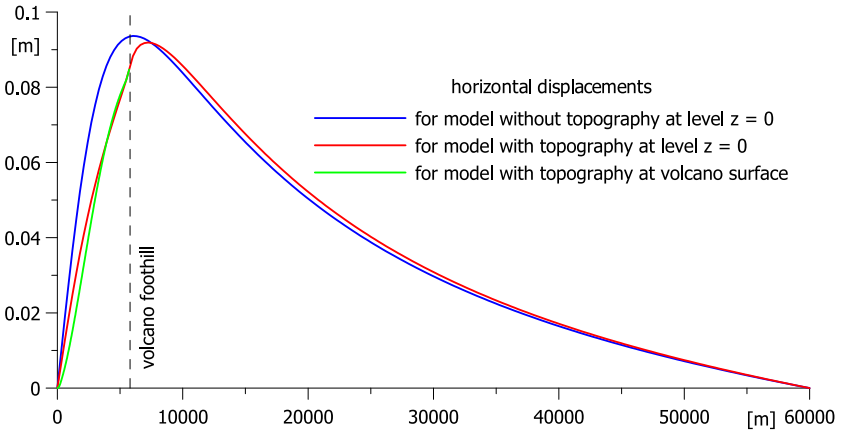

Fig. 8. The comparison of the horizontal displacements for the both variants of the model for the level $z = 0$ (m). The 'foothill' marks the horizontal distance where the volcano topography starts.

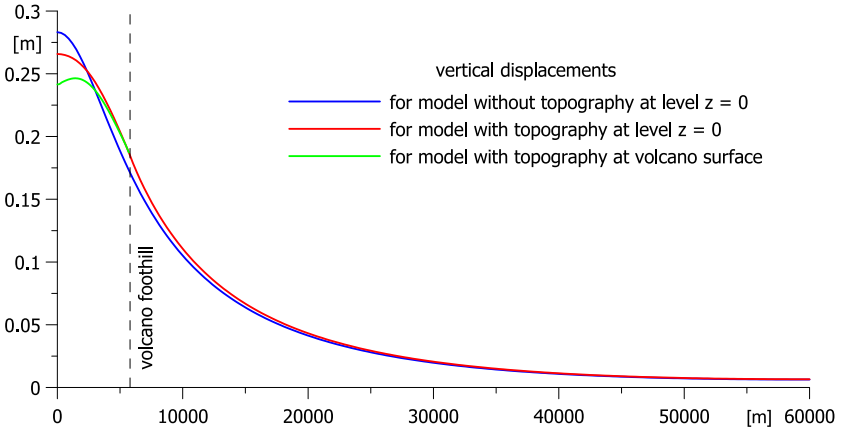

Fig. 9. The comparison of the vertical displacements for the both variants of the model for the level $z = 0$ (m). The 'foothill' marks the horizontal distance where the volcano topography starts.

4. Conclusions

The results show that for the volcanic areas with a pronounced topography the perturbation of the thermo-viscoelastic solution (deformation and total gravity anomaly) due to the topography can be quite significant. In consequence, neglecting topography could give erroneous results in the estimated source parameters. The methods described in this work can be very suitable to more complex models that consider sources of different geometries and allow elastic properties of the medium to vary with depth. While the analytical approximate methodology can be very attractive for solving the inverse problem, the numerical method described above can model the realistic topography and non-uniform elastic and thermal properties of the medium.

Acknowledgements. The authors were supported by Vega Grant Agency under project No. 2/0042/15 and by the Slovak Research and Development Agency (contract No. APVV-16-0482).

References

Babuška I., Szabo B., 1990: Finite Element Analysis, N. Y., J. Wiley.

Brimich L., 2000: Thermoviscoelastic models of the deformations and gravity changes due to anomalous source of heat. Acta geod. et geoph. Hung., **35**, 37–48.

Cayol V., Cornet F. H., 1998: Effects of topography on the interpretation of the deformation field of prominents volcanoes: Application to Etna. Geophys. Res. Lett., **25**, 1979–1982.

Charco M., Brimich L., Fernández J., 2002: Topography effects on displacements and gravity changes due to magma intrusions. Geologica Carpathica, **53**, 4, 215–221.

Combs J., Hadley D., 1977: Microearthquake investigations of the Mesa feothermal anomaly. Imperial Valley, Califonia. Geophysics, **42**, 17–15.

Folch A., Fernández J., Rundle J. B., Marti J., 2000: Ground deformation in a viscoelastic medium composed of a layer overlying a half-space: a comparison between point and extended sources. Geophys. J. Int., **140**, 37–50.

Hvoždara M., 1992: Thermo-viscoelastic deformation field due to a point source of heat in the halfspace. Contr. Geophys. Inst. Slov. Acad. Sci., **22**, 48–66.

Hvoždara M., Brimich L., 1991: Thermoelastic deformation field due to magmatic bodies. Contr. Geophys. Inst. Slov. Acad. Sci., **21**, 59–79.

Hvoždara M., Brimich L., 1995: Theoretical models for gravity anomalies caused by thermoelastic deformations in the vecinity magmatic bodies. Cahiers du Centre Européen de Géodynamique et Séismologie, **8**, 337–349.

Hvoždara M., Rosa K., 1979: Geodynamic effects of thermo-elastic stresses due to a linear heat source. In: V. Babuska and J. Plancar (Eds.): Geodynamic Investigation in Czechoslovakia, Bratislava, Veda, 53–63.

Hvoždara M., Rosa K., 1980: Stresses and displacements due to a stationary point source of heat in an elastic half-space. Studia Geophys. Geod., **24**, 51–59.

Irons B., Ahmad S., 1986: Techniques of Finite Elements, Chichester, Ellis Horwood.

Nowacki W., 1962: Thermoelasticity. Oxford, Pergamon Press.

Teisseyre R., 1986: Thermal stresses, In: R. Teisseyre (Ed.): Continuum theories in Solid Earth Physics, Elsevier, Amsterdam.

Williams C. A., Wadge G., 1998: The effect s of the topography on magma chamber deformation models: Application to Mt. Etna and radar interferometry, Geophys. Res. Lett., **25**, 1549–1552.

Williams C. A., Wadge G., 2000: An accurate and efficient method for including the effecst of topography in three-dimensional elastic models of ground deformation with applications to radar interferometry. J. Geophys. Res., **105**, B4, 8103–8120.